Development of a Seismic Snow Streamer and Use of Multi-Offset Reflection for Determining Glacier Ice Properties

By:

José A. Vélez González
B.S, University of Puerto Rico Mayagüez Campus

Submitted to the Department of Geology and Faculty of the Graduate School of
The University of Kansas in partial fulfillment of the requirements for the degree of
Master of Science 2012

_____
Dr. George Tsoflias, Chair

_____
Dr. Ross Black, Committee Member

_____
Dr. Kees Van der Veen, Committee Member

Date of Defended: 12/12/2012

The Thesis Committee for José A. Vélez González certifies
That this is the approved version of the following thesis:

Development of a Seismic Snow Streamer and Use of Multi-Offset Reflection for Determining Glacier Ice Properties

Committee:

_____

Dr. George Tsoflias, Chair

12/13/2012

Date Approved:

Abstract

Glaciers and ice sheets are important to climate research due to their role in controlling worldwide weather and temperature patterns as well as their potential impact in sea level rise. Because of this, scientists are attempting to model large ice sheets and important fast flowing glaciers. These models are limited in large part to the lack of data which govern the nonlinear behavior of ice flow. Seismic data acquisition can provide high resolution data which can be used to extract information of variables like bed topography, ice temperature and preferred ice crystal orientation. But seismic data acquisition in polar environments is challenging. This is mainly due to the labor intensive process of manually hand planting geophones. In order to improve the efficiency of active source seismic reflection data acquisition in polar environments, two prototype seismic snow-streamers were constructed for this investigation and optimized for deployment in remote locations. The first snow-streamer (experimental snow-streamer) was field tested in the Jakobshavn Glacier located in central western Greenland. The experimental snow-streamer was equipped with multiple geophone configurations and two plate materials. Twenty-two variable angle records were collected using the stationary snow streamer in the center of the survey. The source consisted of 0.5 kg of explosives buried 10 m below the snow surface at 160 m intervals. The resultant data set consisted of offsets ranging from -1760 to +1600 m and the ice-bed interface as well as two internal ice layers were imaged at approximately 1.85, 1.5 and 1.7 km depth respectively. The snow-streamer data was simultaneously collected with a mirror arrangement of hand planted buried geophones in order to test for the effects of plate weight, wind noise, geophone burial and plate to snow coupling in the seismic signal. The signal analysis and the comparison of streamer vs. buried geophones showed that geophone burial can degrade

the seismic signal while the wind and signal analysis revealed that the best snow-streamer configuration was a combination of aluminum plates with vertical geophones. Using these results a second 480m full scale snow-streamer was tested in the Thwaites Glacier Antarctica. The snow-streamer data was simultaneously collected with a mirrored arrangement of surface planted and buried geophones. The trace by trace comparison revealed higher signal to noise in the data collected using the snow-streamer when compared to the surface planted and buried geophones. The full scale snow-streamer was easy to maneuver, very light and could be pulled in speeds up to 15 km/h. The use of the snow-streamer proved to be an efficient data acquisition tool, yielding high quality data. Therefore the use of snow-streamers can represent a significant improvement in the efficiency of seismic data acquisition in polar environments opening the possibility of determining important ice column properties for areas of interest.

An important parameter affecting glacier flow is preferred ice crystal orientation. Seismic waves in ice travel up to 5% faster along the c-axis than when travelling perpendicular to it. Therefore, reflected seismic wave slowness (inverse of the velocity) variability as a function of angle of incidence can be used to detect anisotropy in ice crystal orientation. By combining the multi-offset seismic reflection data set acquired with the experimental snow-streamer and a 2D seismic reflection profile simultaneously collected for the same location, we investigated the presence of preferred ice crystal orientation for the area of study on the Jakobshavn Glacier. The combination of both data sets allowed the approximation of the average ray velocity as a function of angle of incidence. Given that the seismic velocity varies as a function of ice crystal orientation, we can use an existing model to relate the variation of seismic velocity as a function of offset to estimate the mean ice crystal orientation for the bed and imaged internal layers in

terms of a conical c-axes distribution. Based on the anisotropy analysis we concluded that the upper 1640 m of the ice column consists mostly of isotropic ice with c-axes distributed over a conical region of 70^{o} from vertical. The lower 300 m of the ice column is characterized by ice with preferred ice crystal orientation. These observations are consistent with laterally extensive complex ice fabric development reported over the same region of Jakobshavn Glacier.

Acknowledgements

I would like to thank all the people who supported me throughout my master degree. In particular, I would like to thank my three advisers Dr. George Tsoflias, Dr. Ross Black and Dr. Kees Van der Veen. I also like to thank the geophysics students of the Geology Department for their support. Great appreciation to the Center for Remote Sensing of Ice Sheets for provided me with the data and continuous funding for my research. Finally I would like to especially thank my girlfriend, family and friends who stood beside me all the time.

Table of Contents

List of Figures

1.0 Introduction

The Greenland ice sheet is the second largest ice mass in the world, covering an approximate area of 1.71×10^6 km^2. The total volume of the Greenland ice sheet amounts to 2.85×10^6 km^3 of ice or equivalent to 7.2 m in sea-level rise (Church et al., 2001). Over the last two decades there has been increased interest in modeling ice sheets and outlet glaciers to predict changes in polar environments. However, there are significant limitations to the accuracy of these models. According to Van der Veen (2007) there is a need for more realistic models that better capture the non-linear behavior of the Greenland and Antarctic ice sheets. The complex ice flow behavior is mainly controlled by the effects of bed topography, ice column thickness, ice temperature, the geologic formations beneath the glacier, the presence of water at the ice/bed interface and the development of deformable ice layers within the ice column (e.g. Csatho, et. al., 2008).

Fast-flowing glaciers such as the Jakobshavn Isbræ in Greenland are of particular interest to polar environment research due to their significance to ice sheet stability. Understanding the flow behavior of fast-flowing glaciers has potential implications to environmental policy decisions. Geophysical imaging can help scientists better understand the behavior of fast flowing glaciers like Jakobshavn. Airborne ice-penetrating radars are commonly used to determine ice thickness over extensive ice sheets and glaciers as well as detecting water at the ice/bed interface (e.g. Gogineni et. al., 2001; Gogineni et. al., 1998). Additionally, ground based ground-penetrating radars (GPR) measurements have been shown to detect ice layers with preferred ice crystal orientation and reflectivity caused by conductivity changes related to acidity (e.g. Matzuoca et al., 2003). Seismic reflection surveys complement radar imaging of ice sheets and are able to image geologic formations below the ice, beyond the imaging capability of radar, as well as extract information about the properties of materials at the ice bed interface (e.g. Peters, et al.,

2012a; Anandakrishnan, 2003). Seismic surveys also provide information of ice column properties such as preferred ice crystal orientation and temperature (e.g. Horgan et al., 2011; Blankenship and Bentley, 1987; Peters et al., 2012b).

However, seismic surveys are ground-based and therefore labor intensive. In conventional polar seismic surveys, geophones are manually buried approximately 0.5 m below the surface and covered with snow to reduce wind noise and increase coupling between the geophone and the snow-surface. This process is repeated over distances of tens of kilometers. Manual planting of geophones significantly increases the cost of multi-channel seismic reflection surveys, mostly in terms of manpower and time required for the deployment of the sensors. Efforts to improve the efficiency of seismic data acquisition in polar environments have included the use of snow-streamers consisting of a towed array of geophones, analogous to marine seismic acquisition (Eiken et al., 1989; King et al., 1996; Sen et al., 1998). These systems were successful in acquiring good quality multi-channel reflection data more efficiently, but equipment cost, poor coupling, susceptibility to wind noise and excessive weight have limited the use of streamers over snow and ice. Therefore there is still a need for improving the efficiency of seismic data acquisition in polar environments.

Preferred ice crystal orientation within the ice column can have a strong influence on the flow behavior of an ice sheet or glacier. Ice characterized by a preferred orientation (crystals aligned optimally for deformation) is about three times softer than ice with crystals oriented randomly (Dahl-Jensen, 1985). Basal glide causes ice crystal rotation and re-crystallization which develops ice crystal fabric (Thorsteinsson et al., 1997; Azuma et al., 1999). Direct

measurements of crystalline fabrics in drill cores obtained in Greenland (Herron and Langway, 1982; Wang et al., 2002) show that the c-axes of ice crystals frequently have a strong preferred orientation. Uniaxial compression laboratory measurements of ice core samples collected in the Dye 3 ice core (Greenland) reveal that ice deformation occurs in the Wisconsin-age ice in the lower 46% of the ice sheet. This entire depth interval is strongly anisotropic, with a vertical c-axis fabric pattern (Shoji and Langway, 1988). However, there is little direct evidence for the spatial extent of this basal layer and how its thickness varies across the ice sheet. This is primarily due to the difficulty of remotely measuring ice crystal-orientation. Typically, crystal fabrics are measured on samples recovered from ice cores. Ice core information provides accurate and high resolution data on ice fabric. Ice core data is limited by discontinuous measurements, one-dimensional data in the immediate vicinity of the sample and drilling cost. Therefore remote sensing methods especially developed for detecting ice column properties like preferred ice crystal orientation can complement ice core measurements.

There are many variables that control glacier flow but for the purpose of this investigation we are going to concentrate on preferred ice crystal orientation. In numerical models the effect of preferred ice crystal orientation can be introduced by a viscosity variable which enhances ice flow velocity (e.g. Van der Veen et al., 2011). But due to the lack of information of ice column properties like preferred ice crystal orientation, scientists are forced to model ice sheets and glaciers by assuming that the ice crystals are randomly oriented. Ice crystal orientation information must be taken into account to generate accurate ice sheet flow models (Gillet-Chaulet et al., 2006). Therefore, there is a need to use sounding techniques to determine the spatial extent of deformable ice layers and increase our knowledge of significant ice column properties such as preferred ice crystal orientation.

Seismic waves in ice propagate up to 5% faster along the c-axis than perpendicular to the c-axis (Bennett, 1968; Bentley, 1971a; Röthlisberger, 1972). Bennett (1968) investigated the propagation of p-waves through mono-crystalline ice and concluded that layers of ice characterized by preferred ice crystal orientation can be treated as a transversely isotropic (TI) medium. Based on this information as well as direct ultrasonic measurements in single ice crystals Bennett, (1968) derived a set of equations that model the seismic propagation velocity through a -10° C ice column at as a function of mean c-axis ice crystal orientation.

In order to improve our knowledge of ice column properties like preferred ice crystal orientation, a seismic reflection profile was acquired at the Jakobshavn Glacier. The analysis of the seismic profile revealed englacial reflectors occurring in the lower 1648-1740 m of the 1950 m ice-column (Horgan et al., 2008). The authors suggested that the best explanation for the englacial reflectivity is complex fabric development which can introduce changes in seismic propagation velocity. In this thesis we used a long-offset common mid-point (CMP) reflection gather, coincident with the reflection profile presented by Horgan et al., (2008), and we employed the method presented by Blankenship and Bentley (1987) to detect zones of preferred ice crystal orientation in the ice column at Jakobshavn Glacier.

This thesis has two objectives:

1) Develop and test a lightweight and inexpensive snow-streamer for efficient acquisition of multi-channel seismic data in polar environments.

2) Investigate the presence of seismic velocity anisotropy and its relation to ice crystal orientation at Jakobshavn Glacier, Greenland.

2.0 Seismic Snow Streamer

2.1 Streamer Background

Seismic data acquisition in polar environments is challenging. This is mainly due to the remoteness of the field sites, the labor intensive deployment of field equipment and the harsh weather conditions. A time consuming task in seismic data acquisition is the manual planting of geophones and movement of the seismic line. As a result, a few attempts of constructing snow streamers have been made using the same concepts as marine streamers where an array of seismic sensors is towed behind a vessel. The first example of data acquisition using a snow streamer dates back to the 1970's (Einnarsson et al., 1977; Kruppenbach and Bedendebender, 1976) but no comparison between conventional hand planted geophones and the snow-streamer was performed. Eiken et al. 1989 used the same streamer configuration to compare the resulting streamer data to that of conventional hand-planted geophones. The streamer was equipped with half-gimballed geophones. These geophones are self-leveling along one horizontal axis and enclosed in an oil filled cylindrical metal casing. Each casing was approximately 20 cm long with a diameter of 4.5 cm and total mass of about 1 kg per geophone. The streamer consisted of a main cable with a central stress member surrounded by a large number of insulated conductors (figure 1A). The snow-streamer was pulled by a tracked vehicle due to the weight and surface drag of the main cable. From a 4 Km-long line using both a snow-streamer and planted geophones, Eiken et al. (1989) showed that the data from the streamer was comparable in quality to the hand-planted geophones. They also demonstrated that the streamer data was more susceptible to wind due to snow impacting the geophones and vibrations in the cable caused by the wind. They concluded that in wind speeds under 12 knots the streamer data quality is comparable to conventional hand planted geophone data. Furthermore, when the snow-streamer was buried in the snow drift, the force necessary to move it increased by a factor of three. This

required the use of a large towing vehicle, which coupled with the cost of the drag cables as well as the half-gimballed geophones largely, increased the cost of the field deployment. Eiken et al. (1989) concluded that the use of the snow-streamer has to be weighed against the cost, the increased productivity and the downtime due to wind noise. Despite the limitations of the snow-streamer design, it was successfully deployed for a number of investigations in polar environments (e.g. Sen, V., 1998; Anandakrishnan et. al., 1995) yielding positive results.

A different streamer design was developed by King and Bell (1996).This streamer used commercially available geophone elements encapsulated in polyurethane and incorporated in 25 m long rectangular sections. Twelve sections were connected to form what resembled a 300 m-long flexible ski (figure 1B). King and Bell (1996) collected several seismic lines using the streamer and conventional hand-planted geophones over a period of two seasons. The analysis of the data showed good quality results. The advantages of the streamer described by King and Bell (1996) over earlier designs include lower drag, lower building cost and the use of a snowmobile for towing instead of a tracked vehicle. The main drawback was greater susceptibility to wind noise limiting data acquisition to wind speeds under 8 Knots and increased transportation difficulty due to the size of the streamer sections.

Given that data acquired using snow-streamers yielded good quality results the use of snow-streamers can significantly improve the efficiency of data acquisition in polar environments. Therefore, for this investigation I tested two new snow-streamers that overcome some of the limitations of previously discussed snow-streamers and are optimized for deployments in remote locations without the use of large towing vehicles.

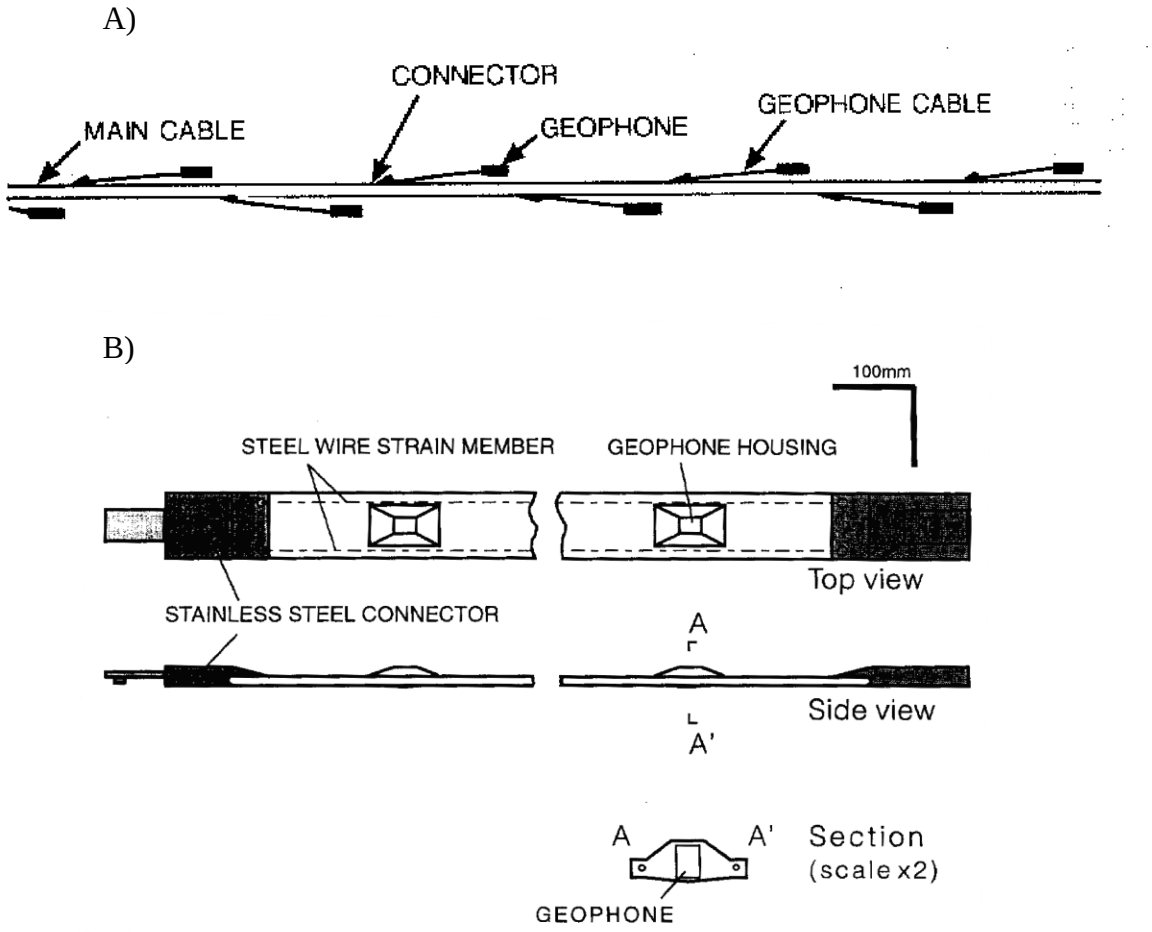

Figure 1: A) Sketch of the snow-streamer system as described by Eiken et al. (1989). B) Snow-Streamer developed by King and Bell (1996).

2.2 Snow-Streamer Design and Testing

2.2.1 Experimental Snow-Streamer Design

The design of the first snow-streamer (experimental snow-streamer) used in my investigation was optimized for deployment in remote locations. Therefore light weight and small size were important factors taken in to account for the design of the streamer. One important design feature was the use of conventional geophones and seismic cables that can be interchangeably deployed as a streamer or conventional hand planted line depending on environmental conditions (e.g. wind speed).

The experimental snow-streamer was composed of eight plates attached to a 7 m long, 20 cm diameter fire hose that served as the towing medium (figure 2A). The plates alternated between aluminum (1.8 kg) and steel (4.5 kg) with 0.5 m spacing between each plate. The experimental snow-streamer was pulled in one direction with an additional steel plate installed in the front of the streamer in order to compact snow and create a smooth surface for the trailing geophone-mounted plates. The use of the fire hose provided several advantages. The fire hose allowed for the cables to be placed inside the hose and provided a low-stretch high strength towing material which prevented the load of the snow-streamer to be transferred to the seismic cables. Additionally the fire hose protected the geophones and cables from wind and snow drift (figure 2 B). Finally, the geophones and cables could be removed and the plates could be rolled together with the fire-hose in a tight and compact package for easy transportation (figure 2 C).

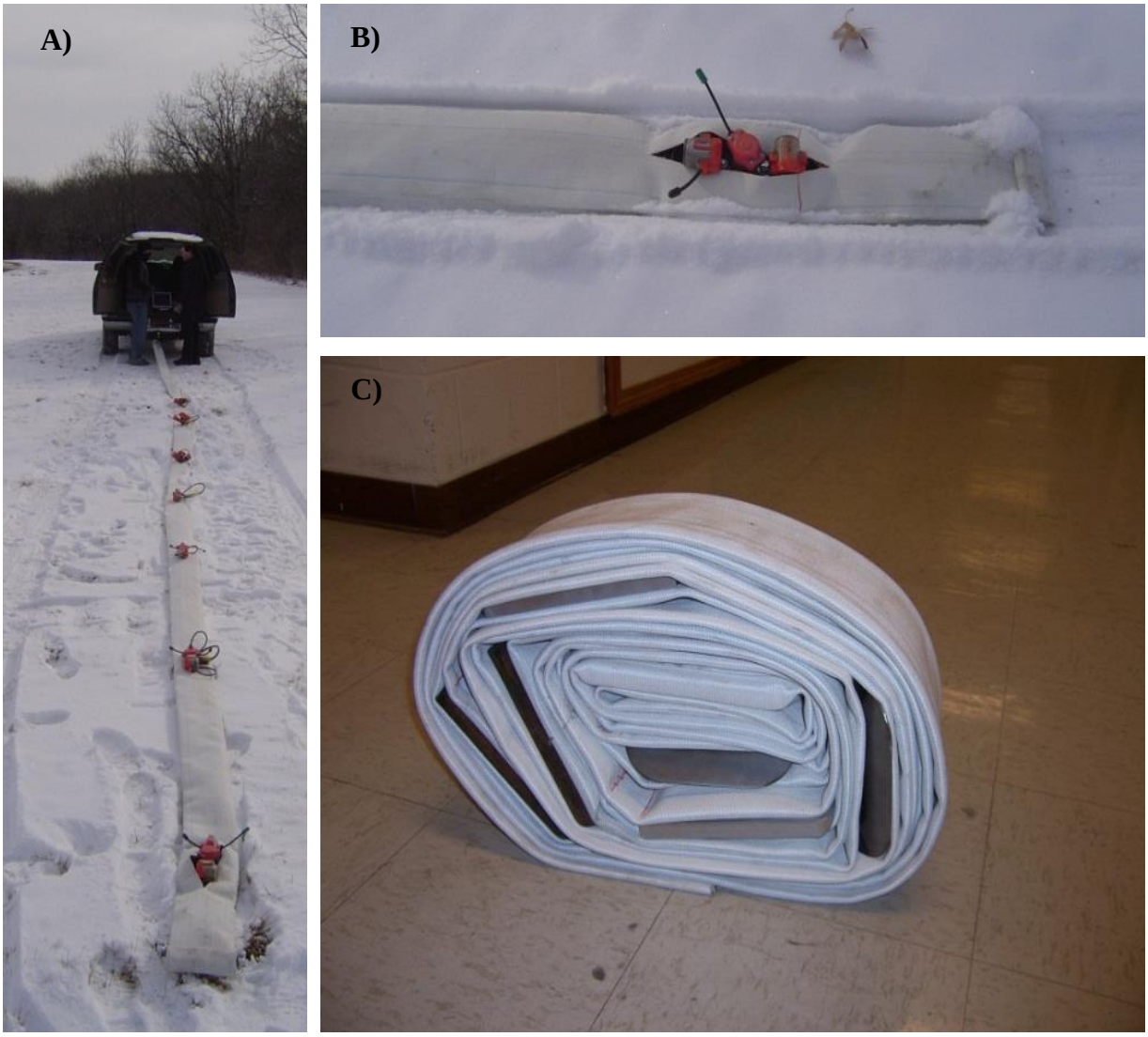

Figure 2: A) Snow-Streamer testing at the University of Kansas. B) Geophones covered with fire-hose. C) Snow-streamer plates and fire hose compactly packaged for transportation.

2.2.2 Streamer Base Plates

To study the effects of weight of the base plate to sensor coupling on the snow surface and the streamer maneuverability two different materials were used, namely steel (4.5 kg) and aluminum (1.8 kg) (figure 3A). The plates were 15.2 cm wide, 1.9 cm thick and 20.2 cm long (figure 3 A - C). The plates were curved in one direction in order to decrease drag and increase the streamer maneuverability. Three 10 mm threads were machined at the top of the aluminum plates and three 10 mm nuts were welded at the top of the steel plates to anchor the towing material and easily mount and dismount commercially available geophones (figure 3 A).

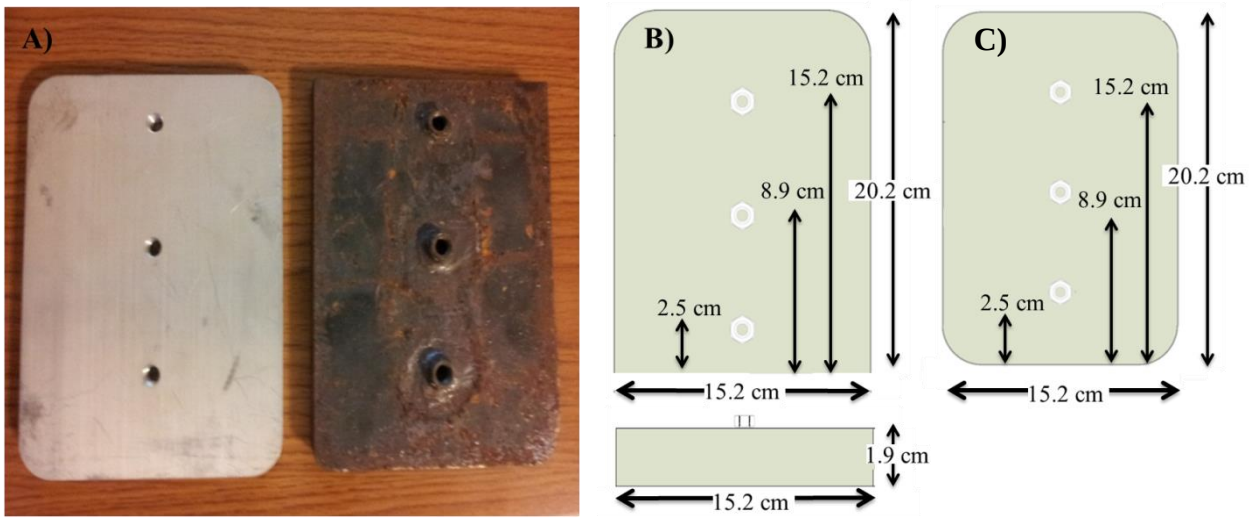

Figure 3: A) Aluminum plate (left) and steel plate (right) used in the experimental streamer. Plate design for snow-streamers deployed at B) Jakobshavn Glacier, Greenland and C) Thwaites Glacier, Antarctica.

2.2.3 Geophones

For the purpose of this investigation we tested several geophone configurations in order to determine the best arrangement for data acquisition in polar environments, taking in to account data quality and susceptibility to wind noise. Four plates (two aluminum and two steel) were equipped with one vertical (100 Hz) and two horizontal (SH, SV, 4.5 Hz) commercially available geophones (figure 4 A). Additionally, four plates (two aluminum and two steel) were

equipped with Galperin (Galperin, 1955, 1974) mounted geophones. Each mounting was equipped with 3 vertical 100 Hz geophones (figure 4 B and C).

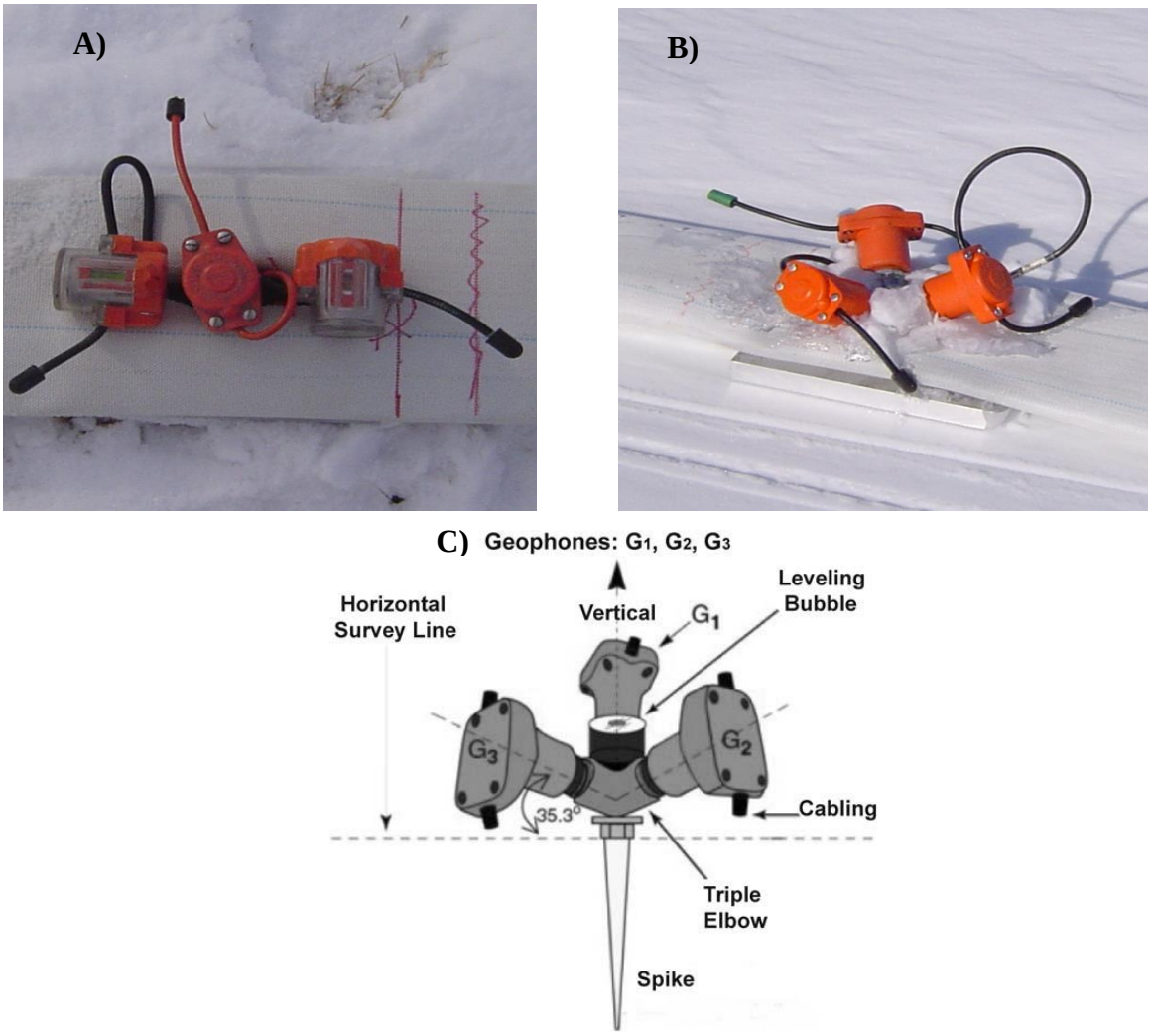

Figure 4: A) Conventional vertical and horizontal (SH,SV) plate mounted geophones. B) Galperin mounted vertical geophones. C) Galperin mounting configuration (Graizer V. 2009).

2.3 Field Testing of the Experimental Snow-Streamer

The experimental snow-streamer was field tested in the summer of 2007 at the Jakobshavn Glacier, Greenland, (figure 5) against a control line of a mirrored-arrangement of hand-planted buried geophones (figure 6). The recording sensors used in the experiment for both the streamer and control line were a combination of vertical (100 Hz), SV and SH (4.5 Hz) as well as Galperin mounted 100 Hz vertical geophones (figure 6). The Galperin mounted geophone data was rotated through an axis transformation in order to obtain the SV, SH and vertical component responses (appendix 1). The data was recorded for 8 seconds with a 0.005 second sampling interval using two 24-channel Geometrics Geode seismographs with simultaneous shot triggering and data recording enabled by GPS synchronization. The seismic source was 0.5 kilograms of pentaerythritoltetranitrate (PETN) placed in shot holes buried 10 meters below the surface.

For this experiment, the recording array of geophones remained stationary and twenty-two seismic sources were deployed at offsets ranging from -1760 to +1600 m with a shot interval of 160 m. In order to assess wind effects and determine the wind cut off threshold of the streamer, the seismic data was recorded under varying wind conditions (0-10 knots: wind speed measured on site using a hand held anemometer). Using the data collected by the experimental snow-streamer at the Jakobshavn Glacier we will:

- Examine coupling to the surface by examining the effect of plate weight and geophone burial on seismic data
- Analyze the effects of wind on seismic data for all geophone configurations using plate mounted and buried sensors.

- Determine if snow-streamers are an appropriate tool for seismic data acquisition in polar environments

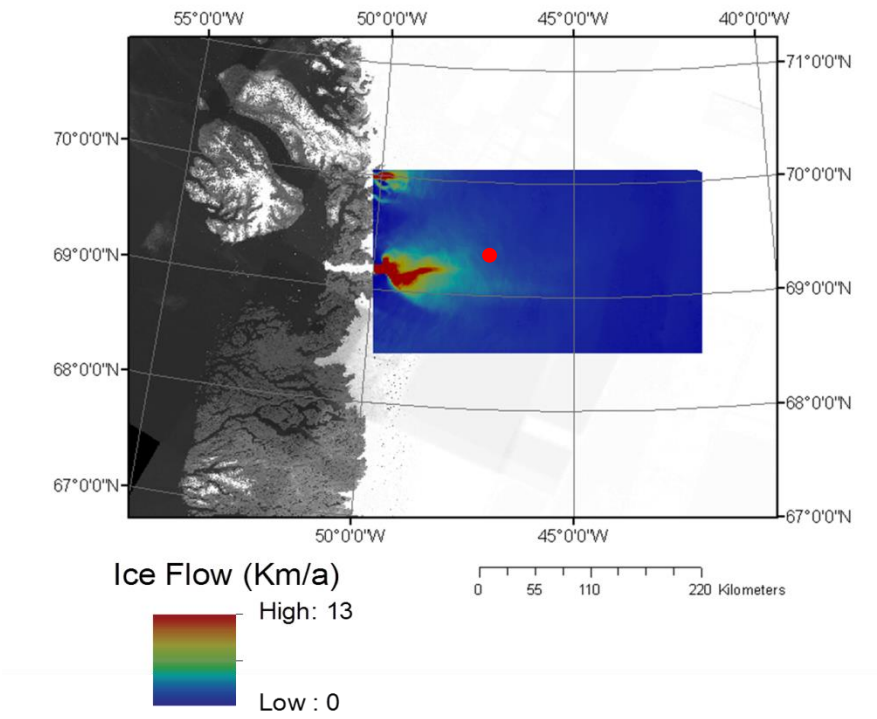

Figure 5: Site location at the Jakobshavn Glacier. Ice flow velocity from Joughin, et. al., 2010.

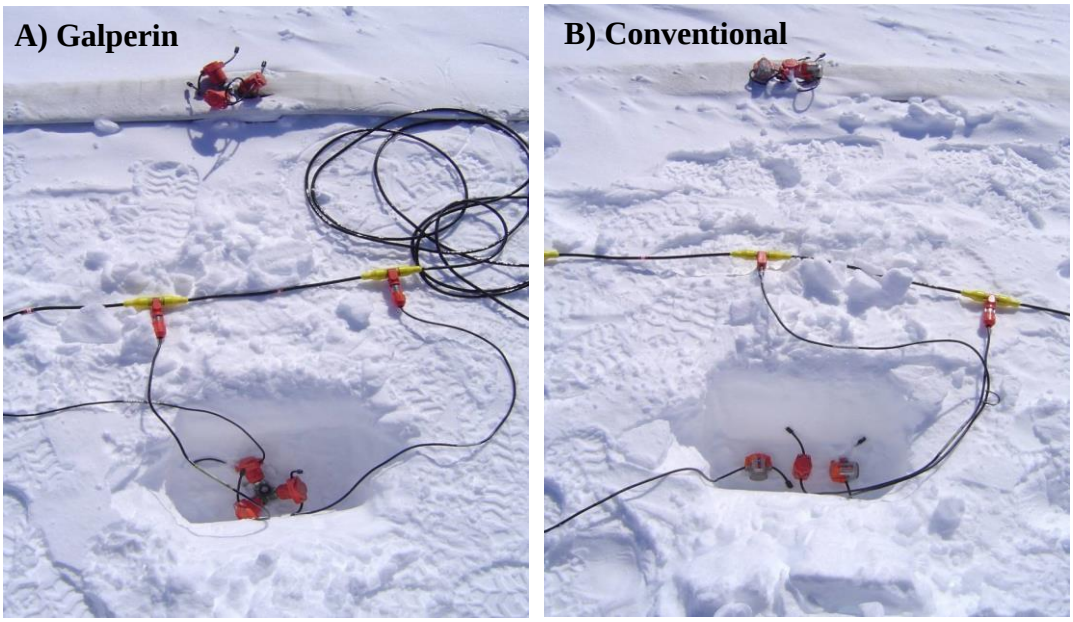

Figure 6: A) Galperin and B) Vertical (100 Hz) and horizontal (SH, SV 4.5 Hz) geophones deployed at Jakobshavn Glacier, Greenland.

2.3.1 Geophone Coupling to Snow: Plate Materials and Geophone Burial Effects

Geophone coupling is affected by a number of variables that include geophone mass, ground to sensor surface area of contact and ground compaction (e.g. Al-Zayer, 2010; Hoover and O'Brien, 1980). Given the importance of coupling to data quality for this investigation, we compare the amplitude and frequency spectra of heavy versus light plates (steel vs. aluminum) in order to assess the effect of sensor mass on the seismic signal.

In polar environments it is common practice to bury geophones approximately 0.5 meters below the snow surface in order to increase coupling and reduce wind noise. But there has never been any studies that tested the effects of burial depth on the seismic signal. To determine whether or not the there is a significant advantage to the practice of geophone burial, we compare the amplitude and frequency spectra of the plate mounted geophones, to surface and buried geophones.

2.3.2 Plate Material Testing Results

The selection of the appropriate plate material is crucial for the streamer design. A plate with excessive weight would be difficult to transport while a light plate could be easily tipped over while pulling the snow-streamer. Therefore it is necessary to test the effects of plate materials on the seismic data and the streamer maneuverability. The plates used for this investigation were made of steel as well as aluminum. The reason for studying steel and aluminum plates was to test for the effects of heavy versus light plates in terms of signal strength and coupling.

The comparison of aluminum versus steel plates, using conventional as well as vertical Galperin geophones reveal that the steel mounted geophones constantly record the greatest signal amplitudes (figure 7). Furthermore, the signal to noise analysis under variable wind conditions (described in section 2.5.1) shows that the S/N values of the steel plates are higher when compared to the aluminum plates for the conventional and Galperin geophones (figure 8).

Recorded seismic amplitudes can be affected by a number of factors (e.g. soil type, soil compaction, geophone mass). Several models have shown that heavier geophones can increase the amplitude response of seismic data (e.g. Al-Zayer, 2010; Hoover and O'Brien, 1980). Given that the data was acquired simultaneously using the same source and equipment, the higher amplitudes can only be explained by the increased mass of the steel plate.

The use of small planes for transportation and snowmobiles as towing machinery, make weight a significant factor to take in to consideration in remote Polar field deployments. Even though the steel plate mounted geophones record greater amplitudes over aluminum plate mounted geophones, steel plates are 2.7 kg heavier. Therefore the use of aluminum plates offers a practical advantage in terms of transportation and deployment.

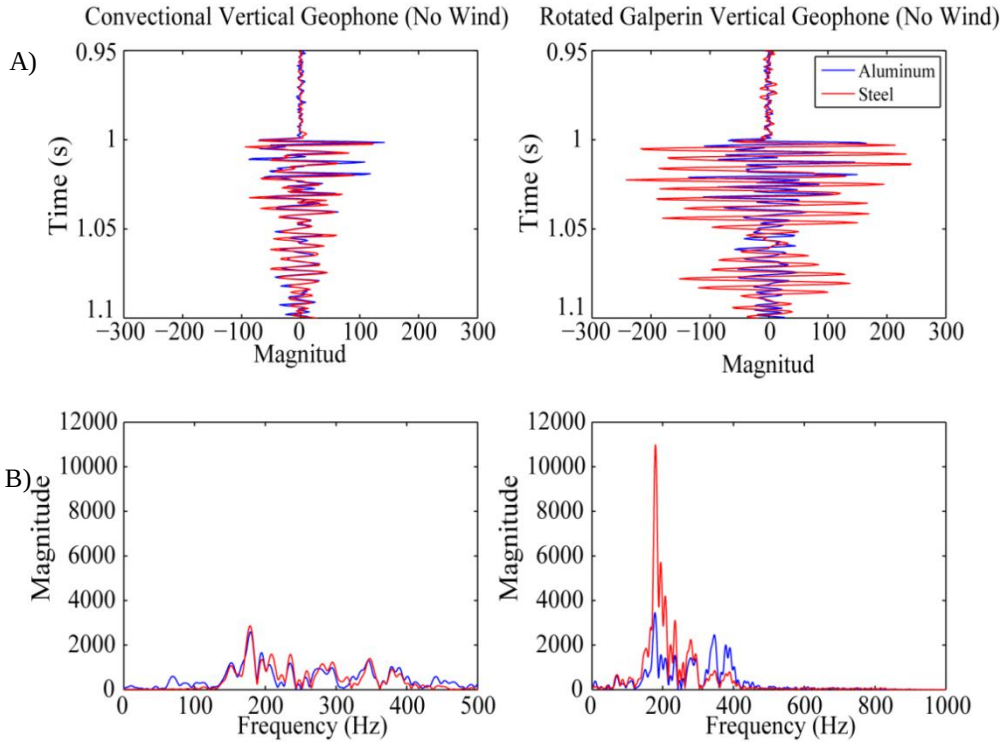

Figure 7: A) Comparison of trace and B) frequency spectra: of steel versus aluminum plate using conventional and Galperin vertical geophone traces under no wind conditions (frequency spectra of data in trace window). A 200 Hz reflection from the bed is recorded at approximately 0.985 seconds two-way travel time.

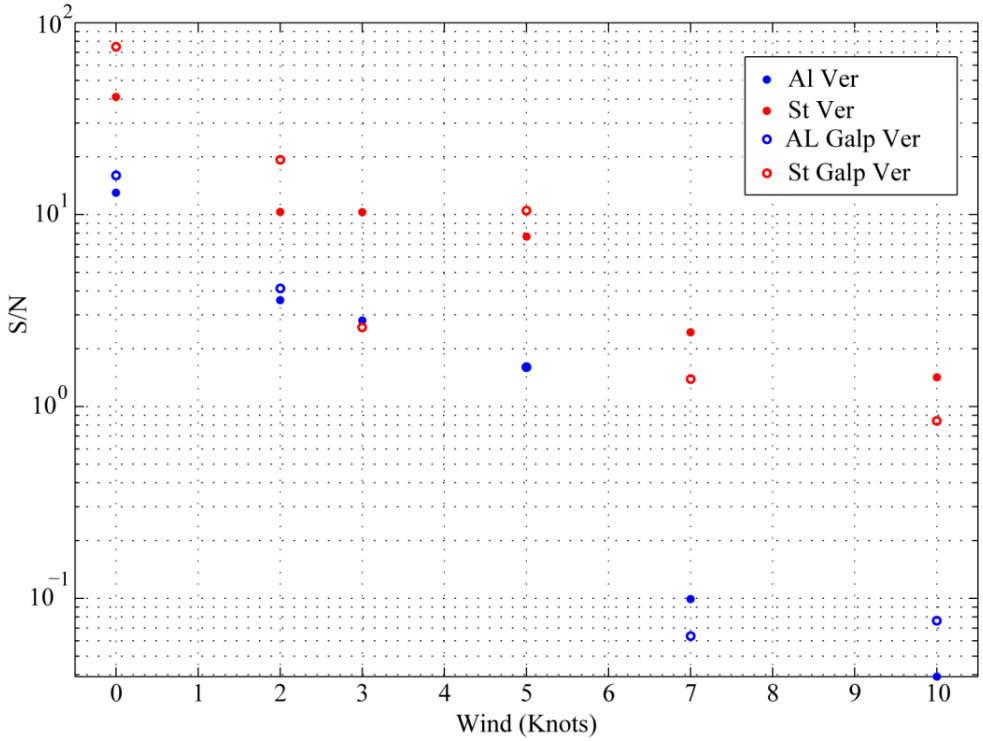

Figure 8: Signal to noise analysis under varying wind conditions calculated for aluminum (blue) and steel (red) plates using conventional (solid circles) and Galperin (open circles) geophones.

2.3.3 Results of Burial Effects on Geophone Response

In polar environments geophones are traditionally placed approximately 0.5 m below the surface and covered with snow to provide maximum coupling and protect the geophone from wind and snow drift (figure 6). The practice of geophone burial is common in polar seismic data acquisition, but no studies testing the effects of geophone burial to the seismic signal have been performed. Figure 9 shows a comparison of data collected using a streamer vertical geophone mounted on an aluminum plate resting on the snow surface, a spiked geophone placed on the snow surface, and a spiked geophone buried ~ 0.4 m below the surface (Figure 9a). Data from the same source shots was recorded simultaneously by the three geophone configurations shown in figure 9a. Trace by trace comparisons reveals that the plate mounted geophones recorded the highest amplitude signal followed by the surface geophone, with the buried geophones recording the lowest amplitude. This was the case for both internal ice layer reflections and the bed reflection (Figure 9b). The most likely explanation for this phenomenon is a combination of increased recorded amplitude due to the additional mass of the plate mounted geophone on the snow surface (see section 2.4.2) and destructive interference between the upcoming subsurface reflection and down-going surface reflection. As illustrated in figure 9a, the geophone mounted to the plate only receives the upcoming reflected signal; there is no downward component acting on the geophone. In the case of the surface geophone, the sensor receives the upcoming arrival and the down going surface reflection. Since the signal reverses polarity at the snow surface, the interaction between the upcoming and down going signals results in destructive interference and reduction of the recorded signal amplitude. Using an approximate depth of geophone burial of 0.4 m and a near surface snow p-wave velocity of 1500 m/s, the time delay of the interaction between the upcoming and down going signals is approximately 0.53 ms. This time delay

corresponds to approximately 10% of a wavelength shift between the upcoming and down going waves which results in destructive interference and the decrease in amplitude of the buried geophone when compared to the surface an plate mounted geophones (figure 9B).

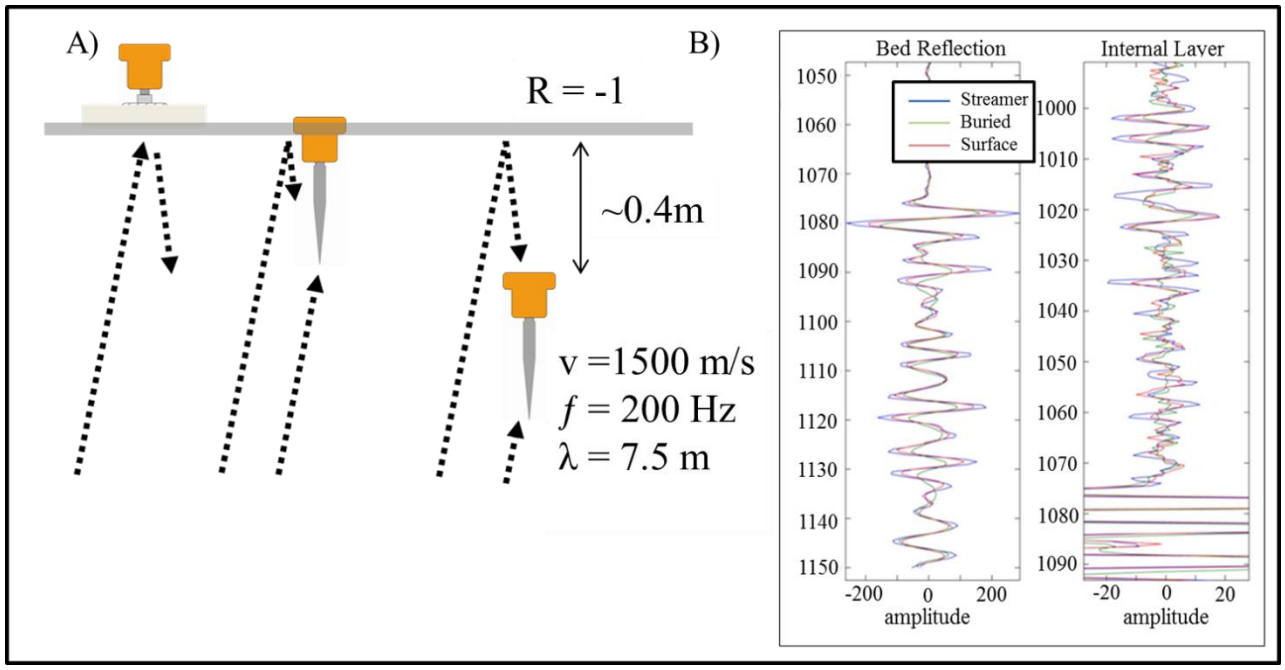

Figure 9: Effects of geophone burial on recorded signal strength: A) Visual representation of the interaction of upcoming and down going seismic waves. B) Trace comparison of plate mounted geophones as well as hand planted and buried geophones.

2.4 Wind Noise

2.4.1 Evaluating wind noise on streamer vs. buried geophones

Wind represents a significant challenge for data acquisition in polar environments. Wind can cause seismic cables and geophones to vibrate. Loose snow carried by the wind impacts the geophones and introduces noise to the seismic data. For this reason, the data acquisition cut off point is commonly at wind conditions between 5 and 15 knots, depending on the surface conditions and the amount of fresh snow on the ground. In order to assess the susceptibility of each geophone configuration (i.e. streamer and buried geophones) to wind noise, recorded signal and noise levels were compared for varying wind speeds.

The noise value (N) is determined by computing the root mean square (RMS) amplitude over the last 2 seconds of each 8 second long seismic trace. Only ambient noise is expected to be present in the latter part of the recorded traces. The signal value (S) is calculated by computing the RMS value of a 0.3 second window encompassing the bed reflection around 1 second two-way travel time. We can assess the effects of wind noise on each geophone configuration by dividing the N of each geophone at varying wind conditions by the corresponding N under no wind conditions (N_{NW}). Signal to noise (S/N) was also calculated for each geophone configuration to determine the quality of the seismic signal under varying wind conditions. The N/ N_{NW} and S/N values were calculated using raw data collected with the buried and plate mounted geophones (aluminum and steel). Furthermore, the trace and frequency spectra for buried and plate mounted geophones, for all geophone arrangements, were compared to determine the best geophone configuration for the full scale snow-streamer.

2.4.2 Vertical Geophone Test Results

The performance of the plate mounted vertical geophones was evaluated by comparing it with a control data set of buried hand planted vertical geophones under varying wind conditions. Figures 10 and 11 show the bed (980 ms) and two internal layers (825 ms and 910 ms) very clearly using the vertical geophones. The trace comparison between plate mounted and buried vertical geophones reveals that in all cases the amplitudes (bed and internal layers) recorded using the plate mounted geophones are greater than the amplitudes recorded with the spike geophones (figure 11). Under no wind conditions, this behavior is attributed to the effects of geophone (plate) mass and burial as described earlier in sections 2.4.

The N/N_{NW} analysis of the seismic data under varying wind conditions revealed that the vertical plate mounded geophones are more susceptible to wind noise when compared to the buried geophones (figure 12). The S/N analysis reveals that the signal to noise ratio for the steel plate mounted vertical geophones is superior when compared to the buried vertical geophones (figure 12). Meanwhile the S/N of the aluminum plate mounted geophones where superior in wind conditions up to 5 knots but less efficient in wind conditions over 5 knots when compared to the buried geophones (figure 12). Furthermore, as seen in figures 10 and 11 in wind conditions over 5 knots it is not possible to clearly image the internal layers. The ice/bed interface was imaged very clearly at the maximum wind speeds occurring at the time of the field deployment (10 knots). In polar environments, the seismic data acquisition cut off point is between 5 and 15 knots. Given that the bed was imaged in all wind conditions, we were not able to establish a data acquisition cut off point for the experimental snow-streamer.

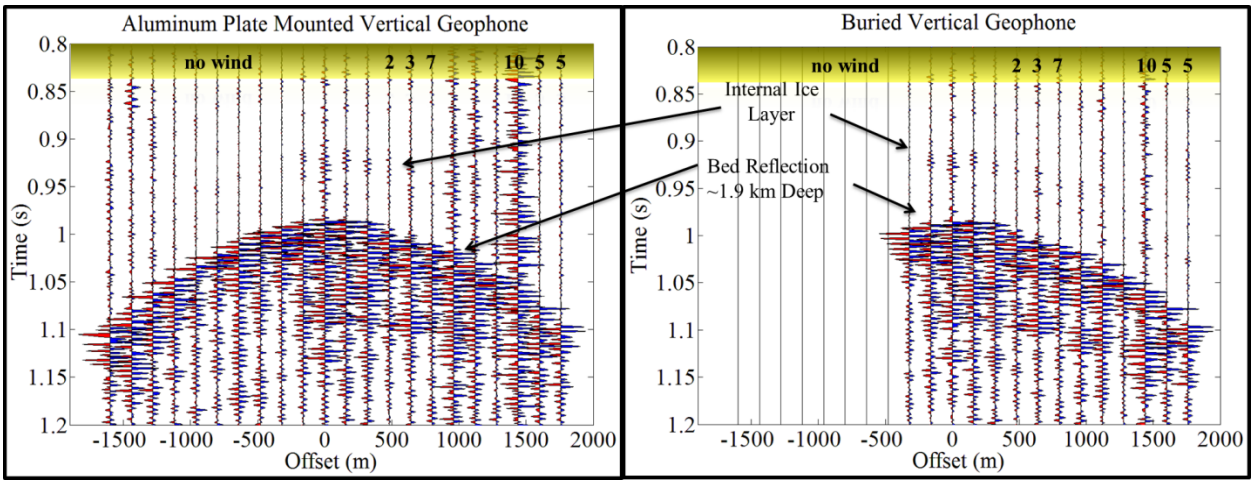

Figure 10: Comparison of surface plate mounted (left) and hand planted buried (right) 100 Hz vertical geophones under various wind conditions.

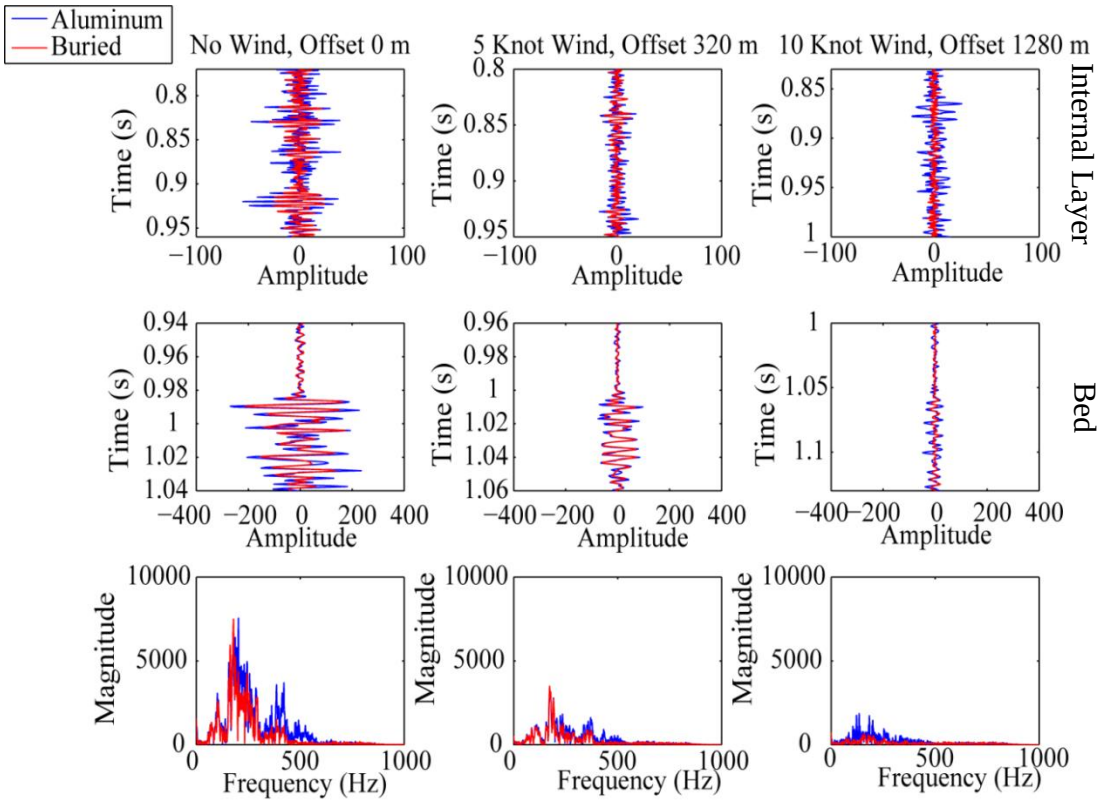

Figure 11: Trace by trace comparison of 100 Hz vertical geophone data under various wind conditions and offsets.

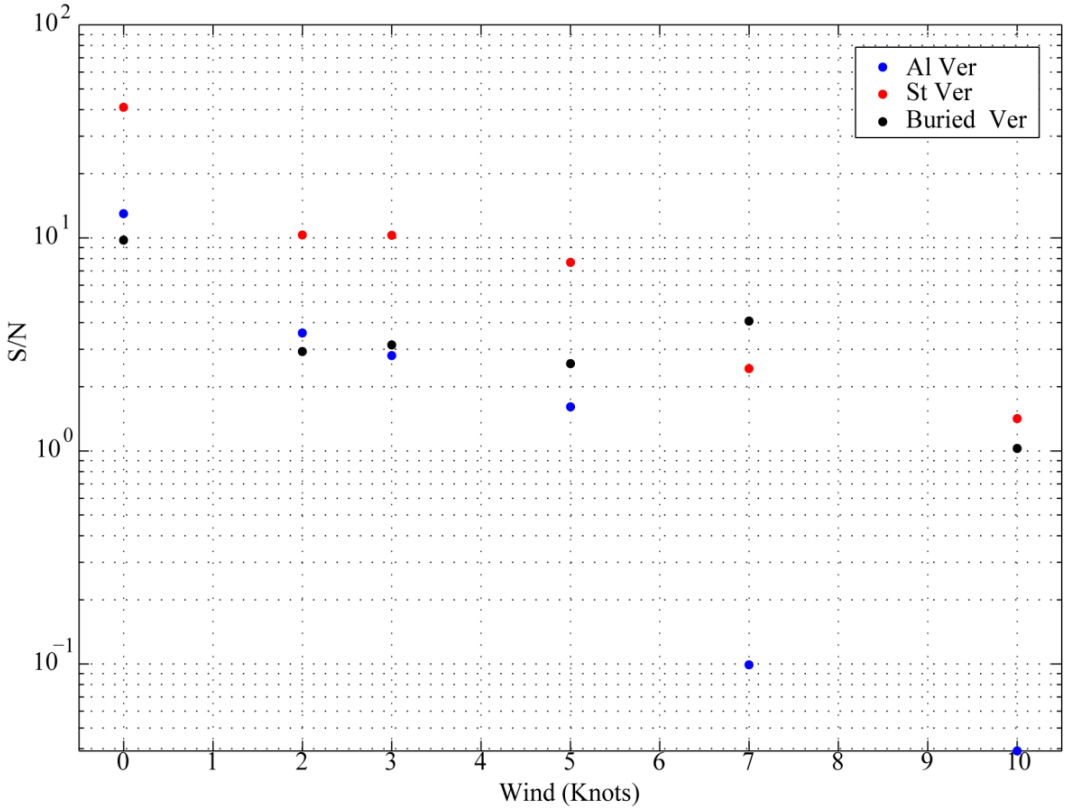

Figure 12: Wind susceptibility analysis of aluminum (blue) and steel (red) plate mounted vertical geophones as well as conventional buried vertical geophones (black).

2.4.3 Horizontal Geophone Results

Horizontal geophones were also tested in this investigation. This type of data is rarely collected in polar environments. The SH and SV geophones record the parallel and perpendicular particle motion of the S-Waves. The comparison of the data from both SH and SV geophones (figure 13) shows a reflection occurring at the same time as the bed arrival recorded on the vertical geophones (figure 10). Assuming a horizontal interface, P-waves can convert to S-Waves and the reflected signal would appear as the SV component. The reflection recorded in the horizontal geophones arrives at the same time as the P-wave, so we have to disregard the possibility of a converted S-wave that propagates at a lower velocity than P-waves. Therefore, the signal recorded by the horizontal geophones corresponds to a P-wave impinging at an angle to the surface, allowing some of the particle motion to be recorded by the horizontal geophones.

This explains the bed reflection of the far offsets recorded by the horizontal geophones and the lack of reflected signal in the near vertical offsets. Further examination of the horizontal component data shows that no converted S-waves were recorded at times corresponding to 1.5 the arrival time of P-waves nor S-waves at twice the P-wave arrivals.

Another important aspect in the evaluation of the data quality of the horizontal geophones is their susceptibility to wind. The elements in the SH and SV geophones are oriented parallel to the snow surface. Wind could also travel in the same direction as the elements in the horizontal geophones. This would result in the introduction of excessive wind noise in to the seismic signal. As seen in figure 13, both geophones were severely affected by wind noise over 5 knots when compared to the vertical geophone data shown in figure 10.

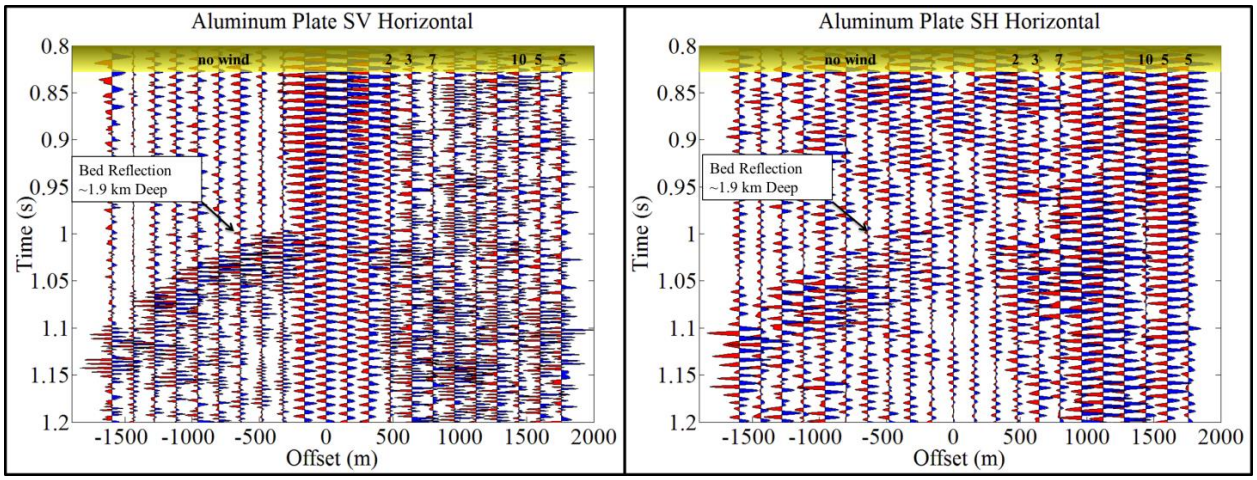

Figure 13: Comparison of horizontal SV (left) and SH (right) geophones under various wind conditions.

2.4.4 Galperin Geophone Test Results

The Galperin mounting allows geophones to record all three components of the incident wave field. Galperin recorded data can be transformed to obtain vertical, SH and SV ground motion (Appendix 1). A comparison between the conventional vertical and Galperin plate mounted geophones reveal that both data sets imaged the bed and internal layers in wind conditions under 5 knots, with the bed imaged in wind conditions up to 10 knots (figures 14-15). The noise analysis as well as the comparison of the trace and frequency spectra reveals that the Galperin geophones are more susceptible to wind when compared to the buried and plate mounted vertical geophones (figure 14 and 15). The signal to noise analysis shows that the steel base plate with Galperin mounted geophones has the best signal to noise in wind conditions up to 5 knots. The steel-Galperin configuration is the heaviest one, with a total weight of 5.0 kg. The increased signal due to the effect of weight (see section 2.4.2) accounts for the additional signal to noise in the steel Galperin geophones (figure14 and 17). The S/N of the transformed vertical geophones after 5 knots was diminished when compared to conventional or plate mounted geophones. This effect is mostly attributed to the additional exposure to wind caused by the Galperin mounting (figure 4C). The additional wind noise exposure is especially evident in the data from the rotated horizontal SH and SV Galperin components (figure 16) were the bed reflection was recorded in wind conditions up to two knots. Given the additional susceptibility to wind caused by the Galperin mounting we do not recommend de use of Galperin geophones for data acquisition in polar environments.

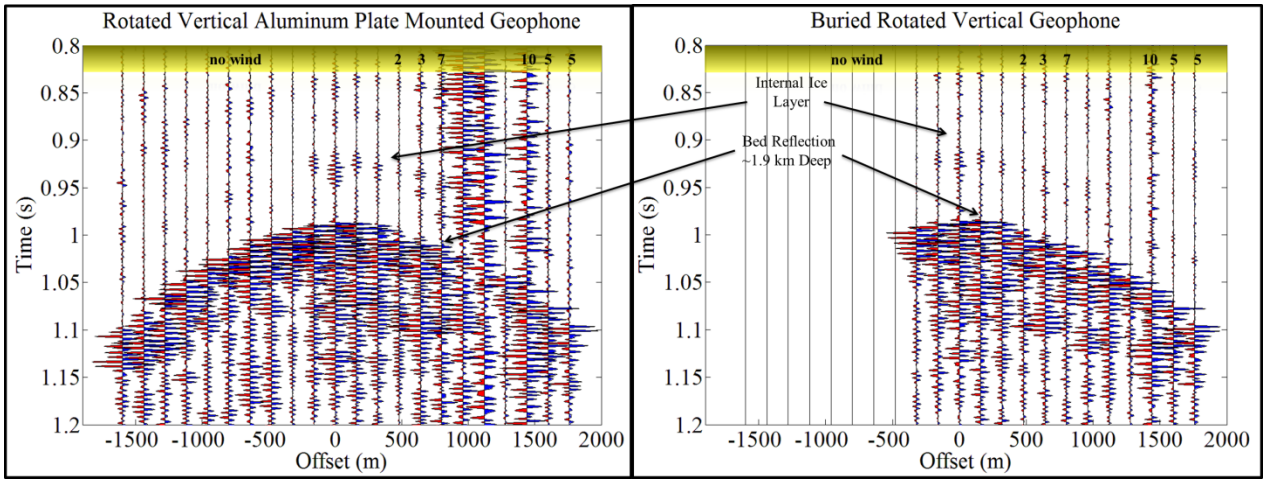

Figure 14: Display of the vertical component data recorded by 100 Hz Galperin mounted geophones on aluminum plate under varying wind conditions.

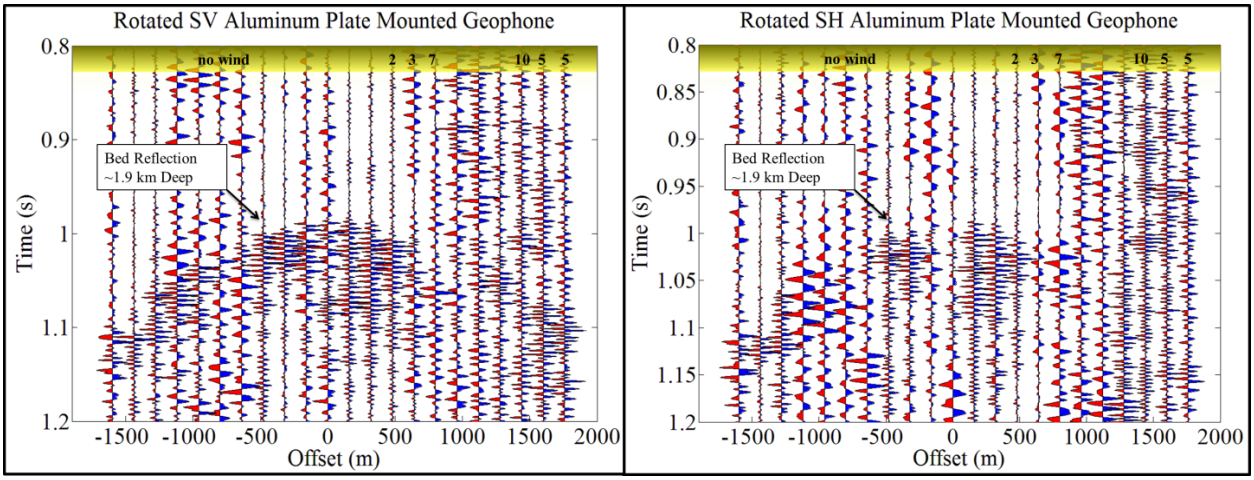

Figure 15: Comparison of rotated SV and SH aluminum plate mounted Galperin geophones under varying wind conditions.

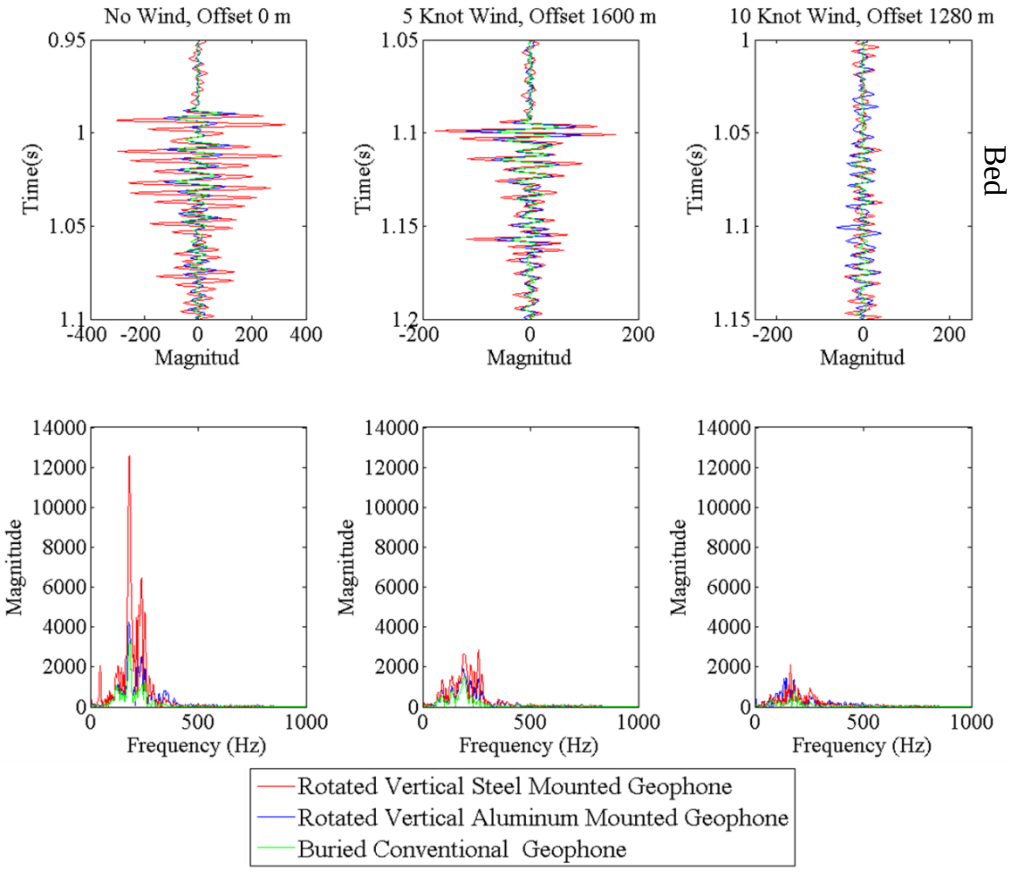

Figure 16: Comparison of rotated 100 Hz vertical aluminum and steel plate mounted geophones as well as conventional buried 100 Hz vertical geophones under varying wind conditions.

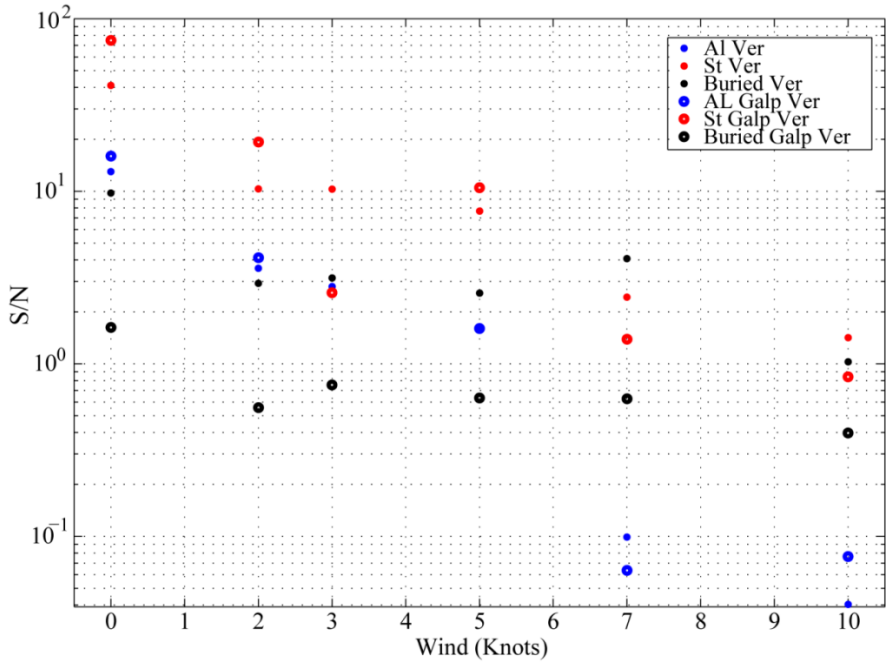

Figure 17: Wind susceptibility analysis of aluminum (blue) and steel (red) plate mounted vertical geophones as well as conventional buried vertical geophones (black) recorded using conventional (solid circle) and Galperin (open circle) vertical geophones.

2.5 Full Scale Snow-Streamer Design

The successful imaging of the bed and internal layers using the vertical plate mounted geophones coupled with the maneuverability and simplicity of the experimental snow-streamer prompted the construction of a second full-scale snow-streamer for efficient data acquisition in polar environments. The full scale snow-streamer was designed to be used for deployments in remote locations in order to image large areas. Therefore the full scale snow-streamer needed to be longer, lightweight and easy to transport. In traditional seismic polar data acquisition, 2D seismic lines are collected in the scale of tens of kilometers (e.g. Horgan et al., 2008; Horgan, et al., 2011). For this reason the full scale snow streamer was built using 24 channel seismic cables with 20 m spaced take outs for a total length of 480 m.

The towing material used in the experimental snow-streamer was a fire hose. But, based on the weight of the fire hose used for the experimental snow-streamer (15 kg) the total weight of the fire hose for a full snow-streamer would be approximately 1030 kg. Given the excessive weight of the fire hose a new towing material was necessary.

Using a force gauge we gradually applied a load and measured the percent of stretch for cargo webbing, marine rope, climbing rope and diving webbing (fire hose was not tested due to excessive weight). As seen in figure 18, the best material would be the marine rope followed by the two webbings. Although the marine rope had a smaller stretching rate, the diving webbing was less expensive and more convenient for the attachment of geophones due to its flat surface. Because of this, the diving webbing was selected as the best towing material.

The base plate material used for the construction of the full scale snow streamer was aluminum. This material was selected to maintain the total weight of the snow-streamer low, in

order to make transportation easier. The plates were the same size as the first streamer but curved in both directions (figure 3B and 19). This enabled the streamer to be pulled in both directions limiting the necessity to turn the streamer while pulled by the snowmobile. The resultant full scale streamer weighed 64 kg and was transported in two small boxes (43 inches long x 27 inches wide x 20 inches high) as two 240 m sections with 12 plates attached per section, excluding the seismic cables and geophones. The only necessary assembly in the field was the attachment of the seismic cables and the mounting of the vertical geophones. By minimizing weight and maintaining streamer simplicity, the amount of man-power and time for assembly is minimized. Additionally it was possible for the streamer to be pulled by a snowmobile or by hand if needed. The plates were able to carve a smooth path over the snow allowing the streamer to glide very easily over the surface. Additionally, by the use of conventional vertical geophones it is possible to detach the geophones under harsh wind conditions and continue data collection by burying the geophones.

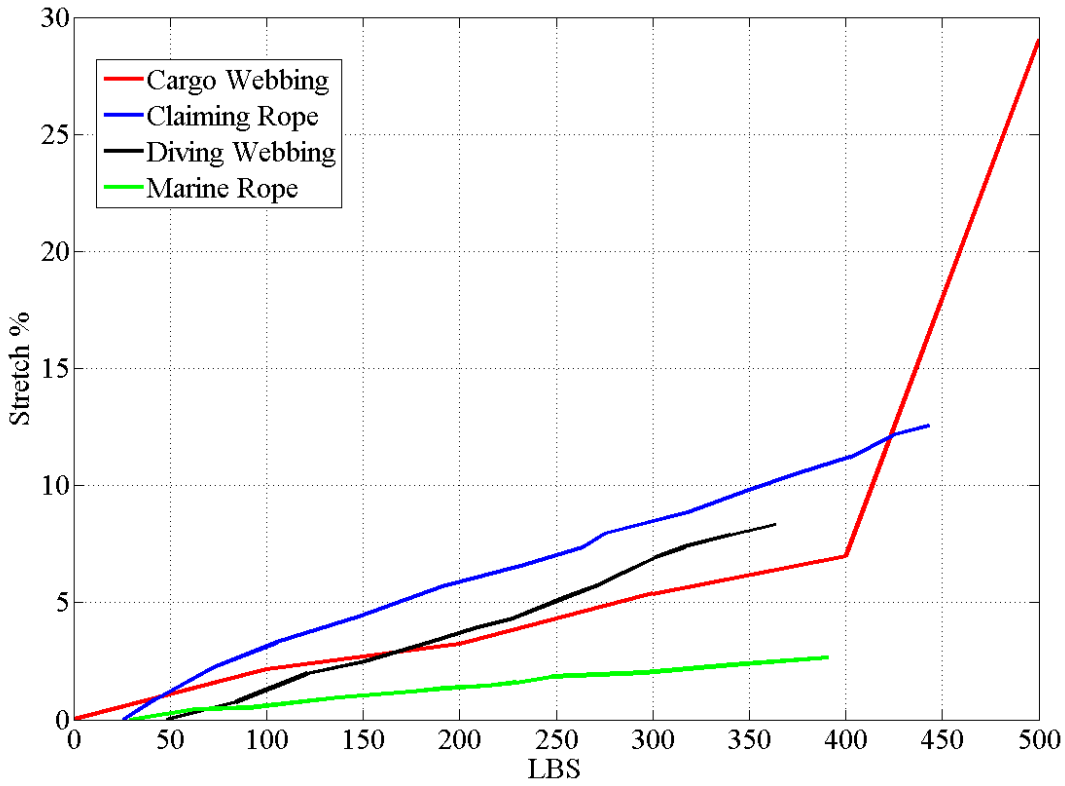

Figure 18: Stretching rates of different towing materials determined by tests performed on samples.

Aluminum Plate with vertical geophone

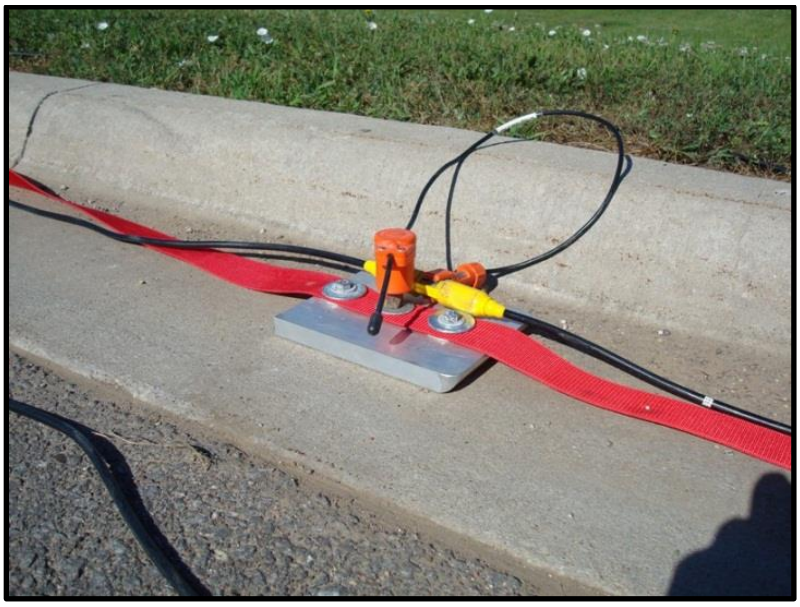

Figure 19: Photograph of a streamer geophone/aluminum plate element, diving webbing used for streamer towing and seismic cable.

2.6 Full Scale Streamer Testing and Results

The full scale snow-streamer was tested in the austral summer of 2008 at Thwaites Glacier Antarctica (figure 20). Due to adverse weather conditions in the area, it was only possible to preform several test shots while the streamer was stationary. The source was one pound of PETN buried 30 m below the surface activated by means of the same trigger system used in Greenland (section 2.3). Three parallel geophone lines (buried, surface and plate mounted vertical geophones) were spaced 1 m apart, each line consisting of twelve 28 Hz vertical geophones at 20 m spacing (figure 21). The data from the snow-streamer was compared to buried and surface geophones under no wind conditions in order to determine if the full scale snow-streamer is an appropriate tool for seismic data acquisition in polar environments.

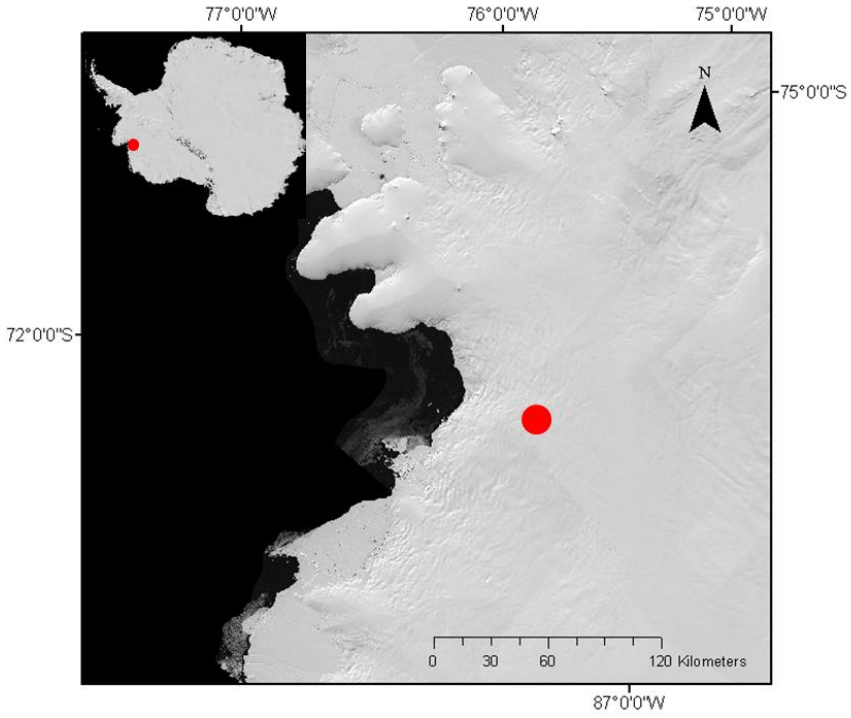

Figure 20: Location of data collection at the Thwaites Glacier Antarctica (LANDSAT, 2007).

The direct trace by trace comparison of the data acquired using the three parallel data lines shows that the maximum amplitude data was recorded using the plate mounted vertical geophones (figure 22). Figure 23 displays all the geophone traces recorded by the three different geophone arrangements under no wind conditions. The data comparison (figures 22 and 23) shows that the best imaging was accomplished with the snow-streamer followed by the surface geophone and last the buried geophones. Burying geophones appears to degrade significantly the seismic signal as discussed in section 2.4.3.

The streamer was easy to transport and assemble in the field. The maneuverability test showed that the streamer had to be pulled at a velocity up to 15 km/h in order to avoid jamming or rolling of plates on the snow surface. Given the high quality of the data collected, the simplicity as well as the low cost and low weight, this snow-streamer could be used as a tool for data collection in polar environments, thus improving efficiency and decreasing man power and cost for field deployments.

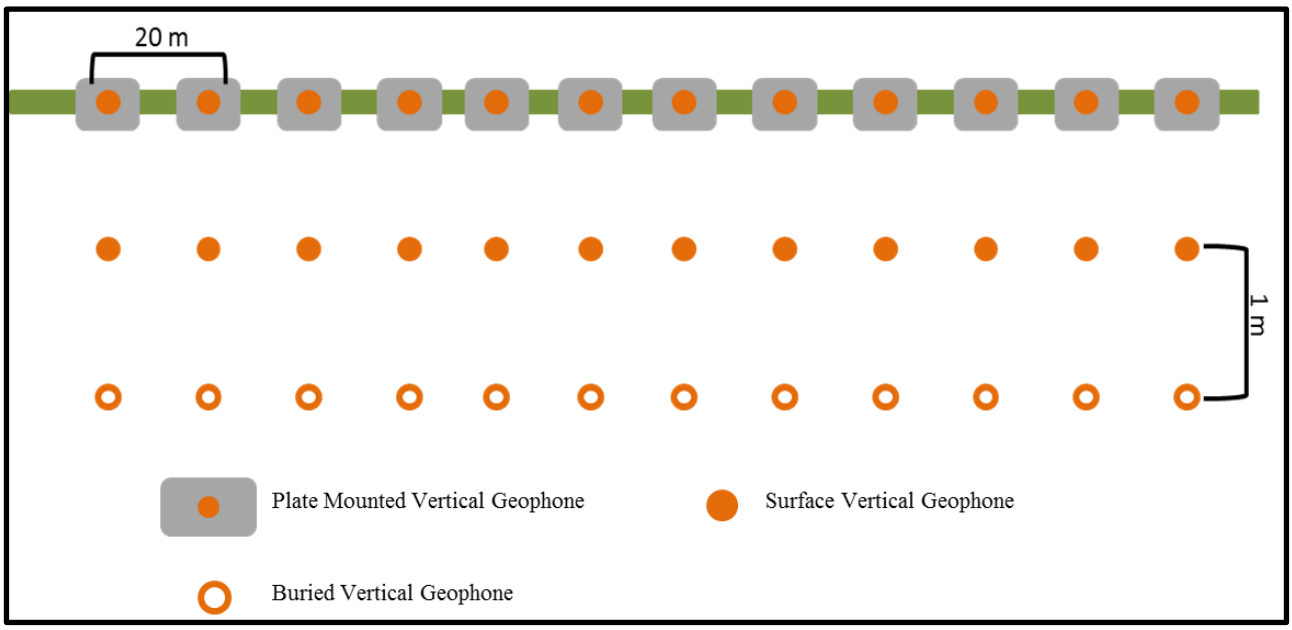

Figure 21: Acquisition geometry of test data collected at Thwaites Glacier Antarctica.

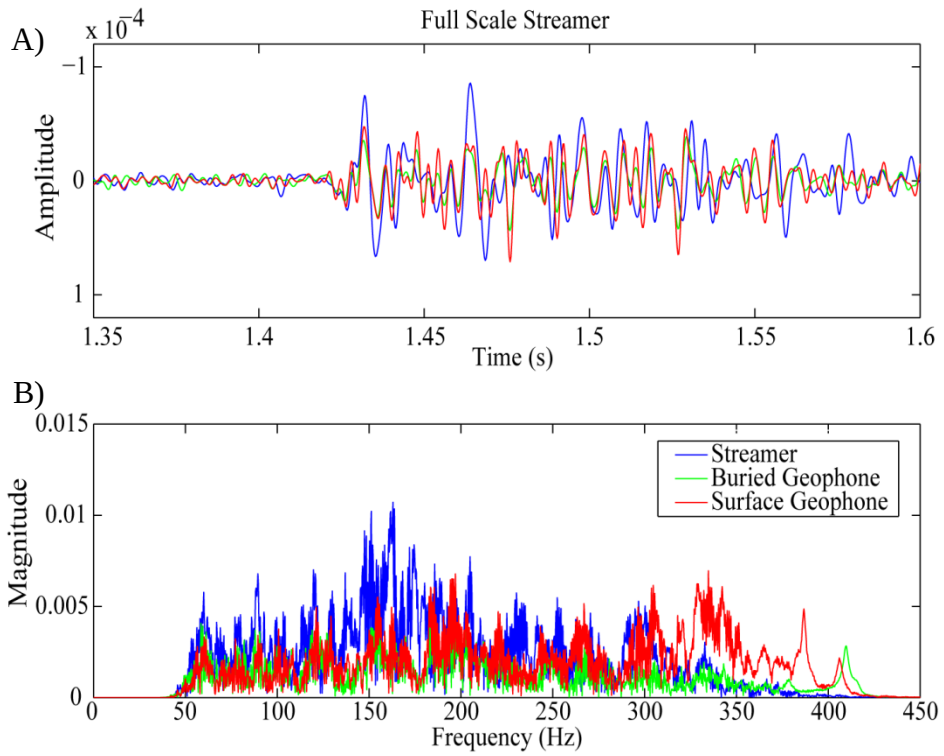

Figure 22: Comparison of trace and frequency spectra of filtered data (Butterworth filter 50 - 350 Hz) collected at Thwaites Glacier under no wind conditions using a combination of plate mounted, buried and surface 28 Hz geophones.

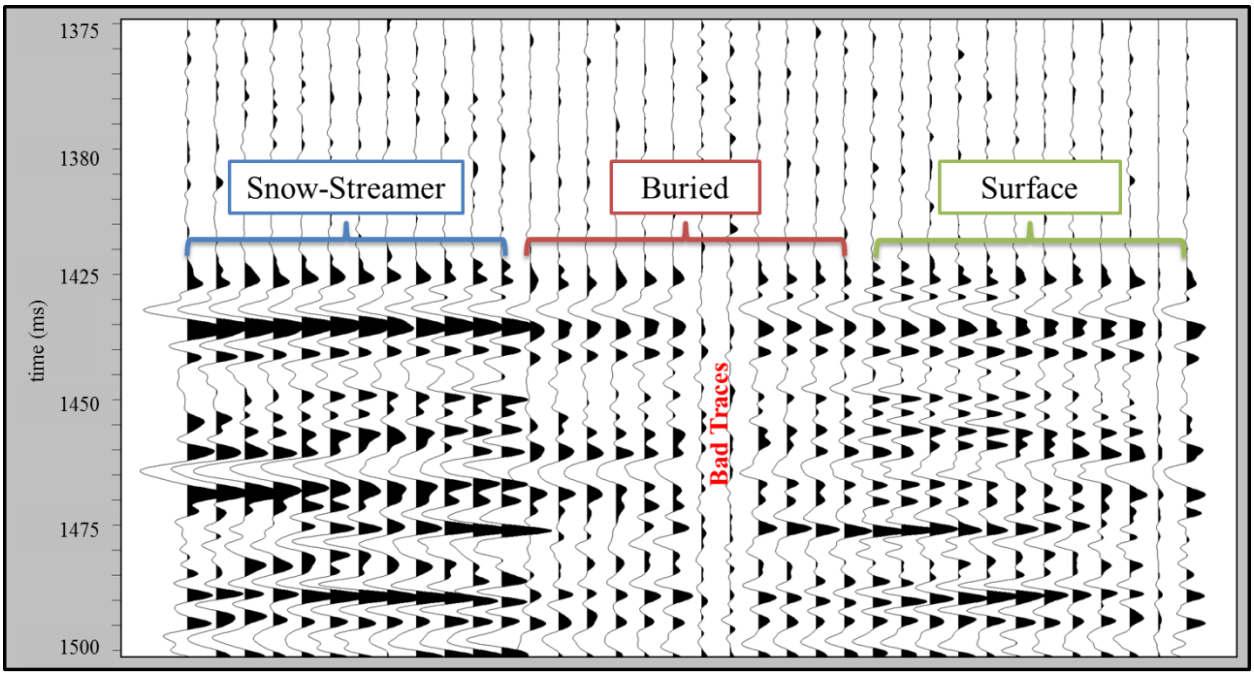

Figure 23: Data collected at Thwaites Glacier under no wind conditions using a combination of plate mounted, buried and surface 28 Hz geophones (Butterworth filter 50 - 350 Hz).

2.7 Snow-Streamer Conclusions

Two snow-streamers were developed in order to optimize seismic data acquisition in polar environments. The experimental streamer was built with the purpose of testing multiple plate materials, snow burial effects and geophone configurations in terms of signal strength and wind susceptibility. In the case of plate materials the analysis revealed that heavier plates, i.e. steel, resulted in greater signal to noise than lightweight aluminum plates and spiked geophones. However, considering that aluminum plate mounted geophones yield adequate signal quality for imaging the bed and internal layers, the additional signal strength does not justify the added weight of the steel plates. Therefore we concluded that aluminum is the best material for plate construction.

The analysis of the multiple geophone configurations reveals that the conventional vertical geophones are the best sensor for streamer construction. Vertical geophones were able to image the bed at 10 knot wind speeds and two internal layers in wind conditions under 5 knots. Horizontal geophones recorded the bed reflection in wind conditions under 5 knots. The arrivals in the horizontal SV and SH geophones occur at the same time as the reflections recorded in the vertical geophones. This reflection is explained by an oblique impinging p-wave field. The arrival of this wave field at an angle would allow some of the energy to be recorded by the horizontal geophones. Although, the horizontal geophones imaged the bed, no evidence of S-waves was found in the seismic records. The lack of S-wave signal coupled to their susceptibility to wind makes the use of horizontal geophones unfit for data acquisition in polar environments. Galperin mounted geophones where rotated in order to recover the response of vertical as well as SV and SH horizontal geophones. Rotated vertical plate mounted Galperin geophones preformed as well as conventional plate mounted and hand planted geophones imaging internal layers in

wind conditions under 5 knots and the bed in wind conditions under 8 knots. The comparison between the conventional and rotated Galperin geophones revealed that the Galperin geophones had the best signal to noise ratio but showed that the Galperin geophones were more susceptible to wind conditions over 5 knots due to the additional exposure caused by the Galperin mounting. Given the results of this investigation, we have concluded that the best configuration for a large scale snow-streamer is aluminum plates with conventional vertical geophones.

Burial effects proved to be a significant factor for data acquisition in polar environments. Direct comparisons of the plate mounted, surface and buried geophones revealed that the recording signal amplitudes decrease with burial. This effect is explained by interaction of the upcoming reflection and down going surface reflected signal resulting in destructive interference. For this reason the practice of burying geophones is only recommended in wind conditions over 5 knots when surface conditions degrade the recorded signal significantly.

Using the results of the experimental snow-streamer a large scale snow-streamer was constructed and tested at Thwaites Glacier, Antarctica. In order to build the optimal snow-streamer several towing materials were tested. It was concluded that the best material was the diving webbing. This material offered the least stretch while minimizing the weight and cost. Twenty four aluminum plate mounted vertical geophones spaced 20 m apart completed the snow-streamer. The comparison between the plate mounted, surface and buried geophones reveal that the maximum amplitudes from the buried geophones are weaker than the plate mounted geophones.

The data acquisition cut off points due to the effects of wind, is dependent on the objectives of the survey. If the objective of the investigation is to image subtle ice column

features like internal layers, the streamer can be used in wind conditions under 5 knots assuming no significant amount of snow drift. If the wind exceeds 5 knots, the geophones can be disassembled from the plates in order to hand plant them and continue acquisition up to wind speeds of 7 knots. If the purpose of the investigation is to image the bed and geological features, the streamer will perform as good as the hand planted geophones. Given that the bed was imaged at the maximum wind conditions of data collection (10 knots), more studies are necessary to determine the wind cut off point for bed imaging.

3.0 Ice Anisotropy

3.1 Background of Jakobshavn Glacier

Jakobshavn Glacier is one of the fastest flowing glaciers on earth and the major discharging outlet glacier in Greenland, draining approximately 7% of the ice sheet (Csatho et al., 2008). Studies from satellite imagery and information from lateral and terminal moraines suggest that Jakobshavn Glacier has experienced significant changes in ice discharge. The retreat of Jakobshavn glacier since 1850, coupled to the collapse of the floating terminus in 1997 (figure 24) was followed by an increase in glacier speed. The speed-up of 6 km a^{-1} in 1995 to over 12 km a^{-1} in 2005 (Joughin et al., 2012) accounts for a total increase in ice flow of 100%, speeds that are sustained today. Given the variation of the terminus position and the importance of this glacier to the stability of the Greenland Ice Sheet, ice flow modelers have tried to explain the recent behavior of Jakobshavn Glacier (e.g. Van der Veen et al., 2011; Thomas, 2004). An important parameter affecting the results of these analyses is the viscosity parameter for ice. This parameter incorporates the effects of temperature and preferred ice crystal orientation. Glacier flow can be strongly affected by the temperature of the ice column with warmer ice deforming more rapidly, resulting in an increase in ice flow velocity (e.g., Hooke, 1981; Huybrechts and Oerlemans, 1988).

Ice crystals are formed by stacking multiple layers of water molecules arranged in hexagonal rings. These layers are called the basal planes of the crystal, and the normal to the basal plane is called the c-axis or the optical axis of the crystal. Preferred c-axis orientation is a result of shear and compressional or extensional stresses induced on the ice column as a response to flow or loading (Hooke, 1998). Ice characterized by a preferred orientation is about three

times softer than ice with crystals oriented randomly (Dahl-Jensen, 1985) and it exhibits seismic velocity anisotropy.

The increase in ice temperature within the ice column can enhance preferred ice crystal orientation, further weakening the ice column. Internal ice column temperature is the result of a complex interaction between the downward advection of surface cold through accumulation, horizontal advection via ice flow, geothermal flux from the geology beneath, and frictional heating due to ice deformation and basal sliding (e.g., Cuffey and Paterson, 2010). Ice temperature can result in a bulk increase or decrease in seismic velocity with in the ice column (e.g., Tonn, 1991; Dasgupta and Clark, 1998; Kohnen, H., 1974). Studies using seismic and ice core measurements show a temperate basal ice layer within the lowermost 14% of Jakobshavn Glacier (Peters et al., 2012; Iken et al., 1993).

A seismic reflection profile acquired at Jakobshavn Glacier revealed englacial reflectors occurring in the lower 300 m of the 1900 m ice-column (Horgan et. al., 2008). The authors suggested that the best explanation for the englacial reflectivity is complex fabric development which can introduce changes in seismic velocity of up to 5%. In this thesis we used a long-offset common mid-point (CMP) reflection gather, coincident with the reflection profile presented by Horgan et. al., (2008), and we employed the method presented by Blankenship and Bentley (1987) to detect zones of preferred ice crystal orientation in the ice column at Jakobshavn Glacier.

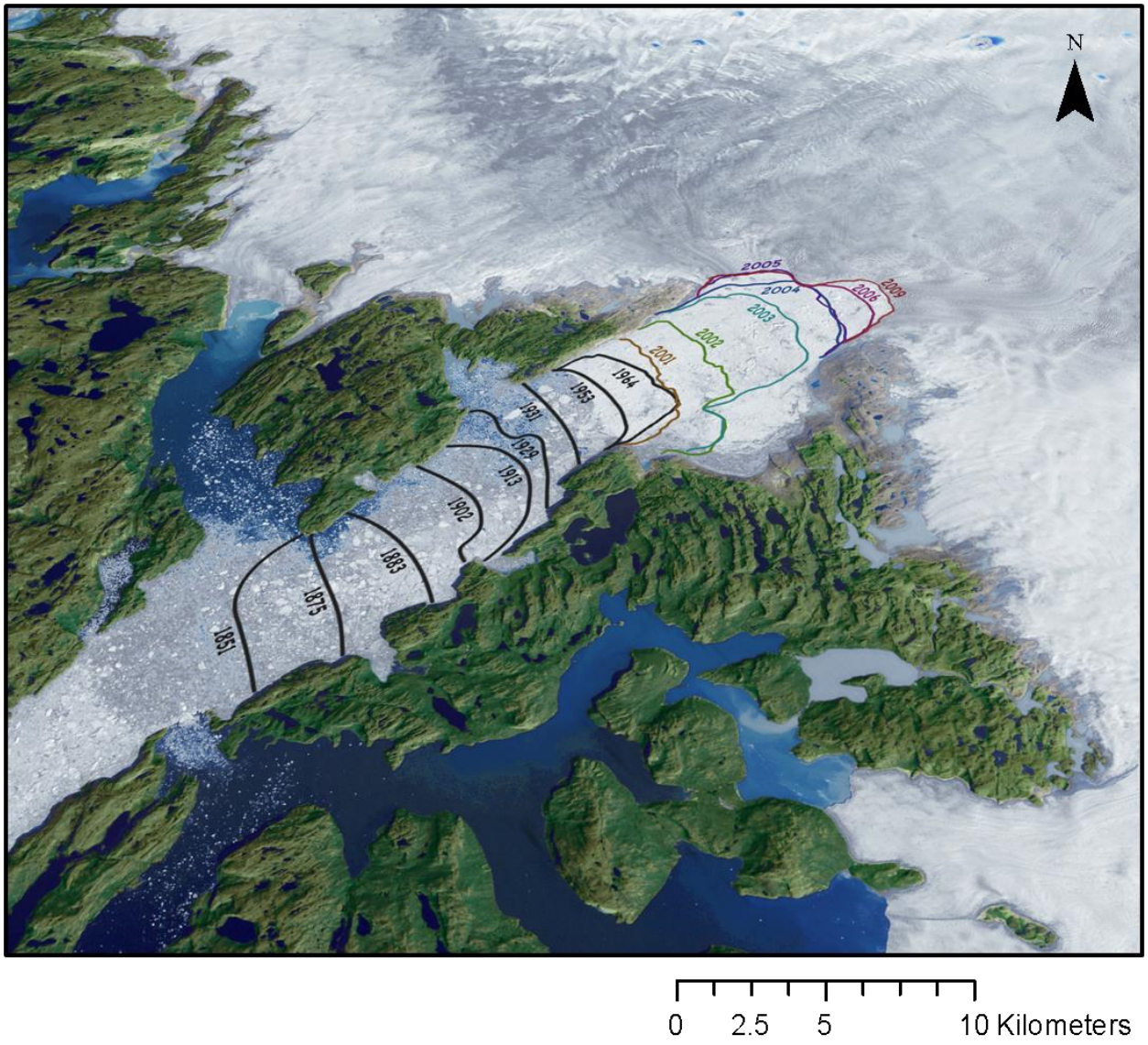

Figure 24: Reconstruction of the Jakobshavn Glacier terminus over 158 years (http://svs.gsfc.nasa.gov/vis).

3.2 Seismic Anisotropy Background

Notation

X, Y, Z = reference coordinate axes (see figure 25).	u, v, w = wave front particle displacement in the x, y, z direction respectively.
σ' = angle of incidence	$\overrightarrow{W}$ = average ray velocity
$\vec{V}$ = velocity vector	$\vec{S}$ = Slowness vector
$\hat{V}$ = velocity surface	$\hat{S}$ = slowness surface
ρ = density	$\hat{v}$ = wave surface
P = stress	e = strain
I = angle of ice crystal orientation in a solid cone distribution	Ψ = represents the change in velocity as a function of angle of incidence
σ = angle between the axis of symmetry Z and the direction of wave propagation	C = elastic modulus

In this chapter I will review the theory developed by Bennett (1968) on seismic wave propagation within ice. The concepts used in the theory of elasticity of solid anisotropic bodies is that of the generalized Hooke's law:

$$P_{ij} = C_{ijkl}\, e_{kl} \qquad (1)$$

where P_{ij} represents nine components of stress, e_{kl} represents nine components of strain and C_{ijkl} represents eighty-one elastic constants. By assuming a body in equilibrium (no rotation of the volume element) the stress and strain tensors become symmetrical ($P_{ij} = P_{ji}$ and $e_{ij} = e_{ji}$). This assumption reduces the number of elastic constants from eighty-one to thirty-six resulting in only six independent components of stress and strain. Although the number of variables necessary to solve Hooke's law has decreased significantly, it is still difficult to practically determine the thirty-six elastic constants using seismic measurements.

Several groups of symmetries are used to control the stiffness of a medium (see equation 1: C_{ijkl}) and consequently the velocity the wave travels through solids (e.g. Isotropic, Monoclinic, Triclinic, Cubic, Orthorhombic and transversely isotropic). These symmetries are distinguished from one another by the form of their tensor (Tsvankin, 2005). The analysis by Bennett (1968) revealed that the type of anisotropy characteristic of hexagonal crystals like ice is similar to that which is predicted for layered media. A medium of this type is called transversely isotropic (TI) and has elastic properties which are radially symmetric with respect to a fixed direction, thus reducing the number of independent elastic constants from thirty-six to five. In the case of layered media, the direction in which the elastic properties are radially symmetric is normal to the layering. As mentioned previously, seismic waves in ice travel up to 5% faster along the c-axis than when travelling perpendicular to it (Bennett, 1968; Bentley, 1971a; Röthlisberger, 1972). Therefore, if an ice column is characterized by ice with preferred crystal orientation, the elastic properties of the ice column would be symmetrical along the c-axis. By combining the stress strain relation of a wave front traveling in a homogeneous TI medium and the equation of small motion we obtain the wave motion of a plane wave front through a TI medium:

$$\rho \frac{\partial^2 u}{\partial t^2} = C_{11} \frac{\partial^2 u}{\partial x^2} + C_{66} \frac{\partial^2 u}{\partial y^2} + C_{44} \frac{\partial^2 u}{\partial z^2} + (C_{12} + C_{66}) \frac{\partial^2 v}{\partial x \partial y} + (C_{13} + C_{14}) \frac{\partial^2 w}{\partial x \partial z}$$

$$\rho \frac{\partial^2 v}{\partial t^2} = C_{66} \frac{\partial^2 v}{\partial x^2} + C_{11} \frac{\partial^2 v}{\partial y^2} + C_{44} \frac{\partial^2 v}{\partial z^2} + (C_{12} + C_{66}) \frac{\partial^2 u}{\partial y \partial x} + (C_{13} + C_{44}) \frac{\partial^2 w}{\partial y \partial z} \quad (2)$$

$$\rho \frac{\partial^2 w}{\partial t^2} = C_{44} \frac{\partial^2 w}{\partial x^2} + C_{44} \frac{\partial^2 w}{\partial y^2} + C_{33} \frac{\partial^2 w}{\partial z^2} + (C_{13} + C_{44}) \frac{\partial^2 u}{\partial z \partial x} + (C_{13} + C_{44}) \frac{\partial^2 v}{\partial z \partial y}$$

$$C_{66} = \frac{C_{11} - C_{12}}{2}$$

The assumption of transverse isotropy implies that the medium is radially symmetric. Thus, the mathematics become a two dimensional problem (Ɛ = 0, therefore all $\frac{\partial}{\partial y} = 0$, see figure 25). The expression of wave propagation on a plane wave field is given by:

$$(u, v, w) = \left(A_x, A_y, A_z\right) e^{-ik(\sin\sigma x + \cos\sigma z - Vt)} \quad (3)$$

where A is the initial displacement amplitude in the (X, Y, Z) direction, k the wavenumber , σ the angle between Z and the velocity vector $(\vec{V})$, as well as the time (t) (figure 25).

By constraining the analysis to only include p-waves and assuming a plane wave as well as combining equations two and three, Bennett (1968) proved that the expression of the phase velocity of the p-wave in anisotropic ice is given by:

$$2\rho V^2 = (C_{11} + C_{44})\, sin^2\sigma + (C_{33} + C_{44})\, cos^2\sigma + \{[(C_{11} - C_{44})sin^2\sigma - (C_{33} - C_{44})cos^2\sigma]^2 + 4(C_{13} - C_{44})^2\, sin^2\sigma\, cos^2\,\sigma\}^{1/2} \quad (4)$$

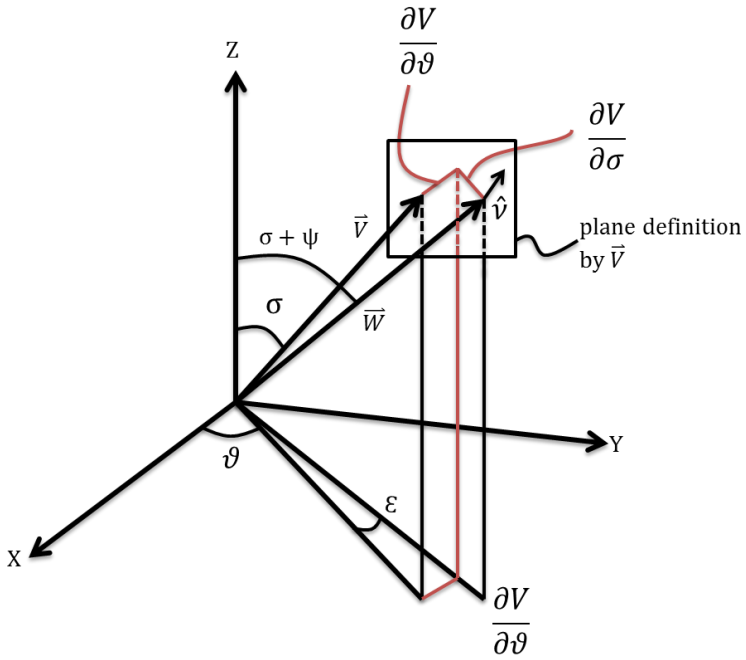

Figure 25: Reference coordinate system (Bennett, 1968).

A velocity vector $\overrightarrow{V}$ (with magnitude V) expanding outward from the source will define the velocity surface ($\hat{V}$) if we allow the vector $\vec{V}$ to sweep through all possible σ angles. This surface is symmetrical about Z (figure 26). The inverse of the velocity surface will define the slowness surface$\left(\vec{S} = \vec{V}^{-1}\right)$.

The wave surface $\hat{v}$ (better known as the wave front) is defined as the surface over which the phase of a traveling wave disturbance is the same (Sheriff, 2006). The $\hat{v}$ can be constructed by calculating the average ray velocity vector $\overrightarrow{W}$ for each angle of incidence σ'. In a purely isotropic case, the normal to $\hat{v}$ is parallel to $\overrightarrow{W}$. In the anisotropic case, $\hat{v}$ would not be perpendicular to $\overrightarrow{W}$ and the relationship between $\overrightarrow{W}, \vec{V}$ and $\vec{S}$ is given by equation five (see figure 26).

$$\frac{1}{\vec{S}} = \vec{V} = \overrightarrow{W}\cos\psi \qquad (5)$$

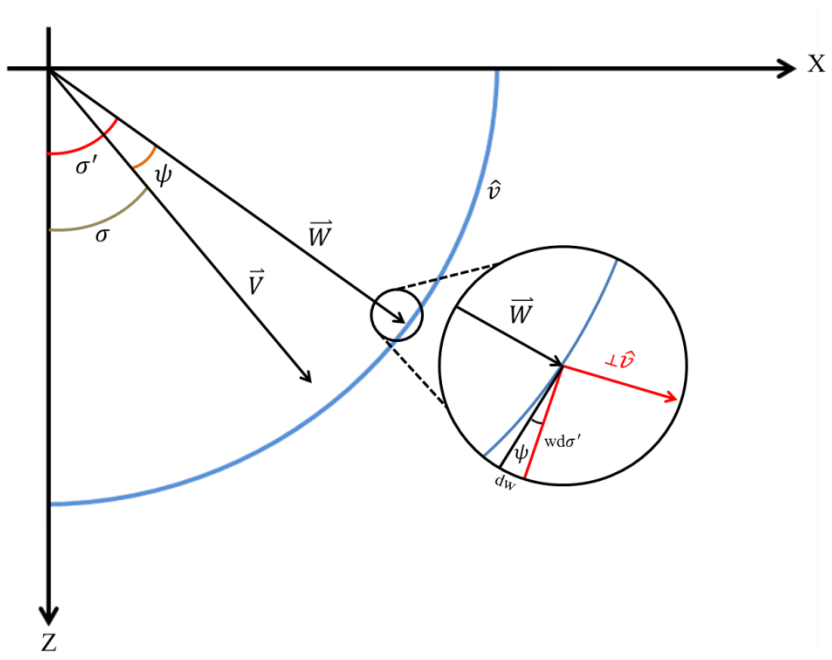

Figure 26: Wave surface and velocity surface interrelationship and notation.

Bennett (1968) determined five elastic constants on single ice crystals obtained from the Mendenhall Glacier in Alaska (ice temperature:-10° C) by means of ultrasonic measurements ($C_{11} = 14.06 \pm 0.08,\ C_{12} = 7.15 \pm 0.15, C_{13} = 5.88 \pm 0.25, C_{33} = 15.2 \pm 0.12, C_{44} = 3.06 \pm 0.034$: $C_{ik}\ 10^{10}\ dynes/cm^3$).

Using his results in equation 4, Bennett (1968) modeled (figure 27) the mean slowness of ice crystals by assuming that the crystallographic c-axes were spaced evenly along a solid cone of semi-apex angles I with radial symmetry about the Z axes (figure 28). The choice of a solid cone was not random. The geometry of the solid cone is frequently observed in core measurements collected in ice sheets (Blankenship 1982). The expression for mean slowness was obtained by space averaging the slowness contribution of each single ice crystal orientation. According to Bennett (1968) the expression of a slowness surface on a solid cone for mono-crystalline ice at -10° C is given by:

$$S(\sigma, I) = A + B\cos 2\sigma + C\cos 4\sigma \tag{6}$$

$$A = \left\{a - \frac{1}{3}b - \frac{1}{15}c\right\} + \frac{1}{6}\left\{b - \frac{23}{20}c\right\}(\cos I + \cos^2 I) + \frac{9}{40}c(\cos^3 I + \cos^4 I)$$

$$B = \frac{1}{2}(b - c)(\cos I + \cos^2 I) + \frac{1}{2}c(\cos^3 I + \cos^4 I)$$

$$C = -\frac{3}{8}c(\cos I + \cos^2 I) + \frac{7}{8}c(\cos^3 I + \cos^4 I)$$

where a, b, and c are coefficients empirically derived using monocrystaline ice at -10° C (a=256.28 µs/m, b = -5.08 µs/m, and c = -5.92 µs/m), σ is the angle is between the axis of symmetry Z and $\vec{S}$, were I represents the ice crystal orientation in a conical distribution (figure 27-28).

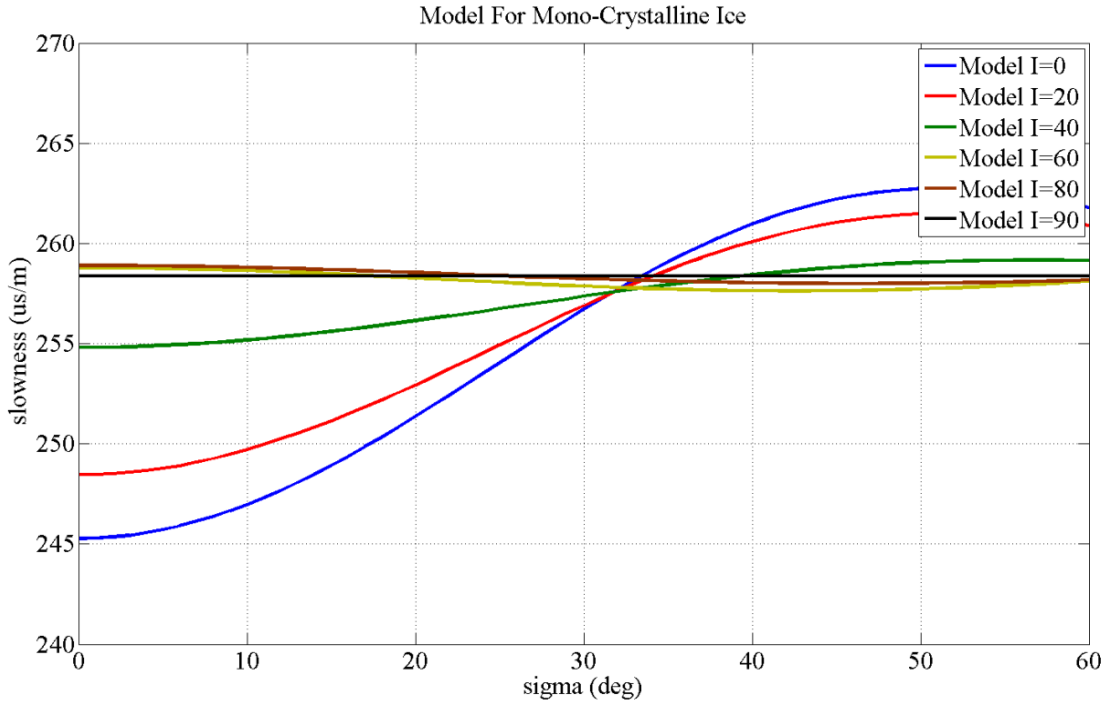

Figure 27: Model for slowness surface on a solid cone for mono-crystalline ice at -10° (from Bennett, 1968).

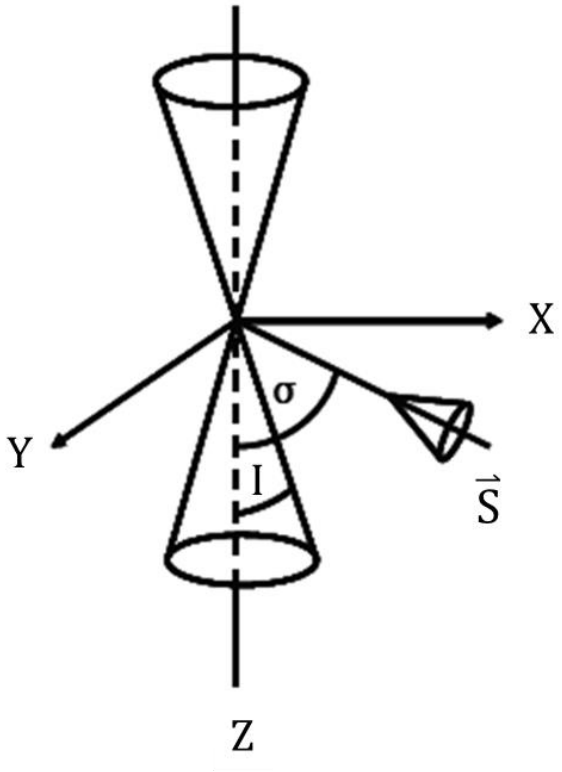

Figure 28: Geometry and notation for a conical c-axis distribution (from Blankenship and Bentley, 1987).

3.3 Calculating Mean Ice Crystal Orientation from Seismic Measurements

In order to determine the slowness variability in multi-offset seismic data, it is necessary to calculate the angle of incidence ($\sigma'_{\pm}$) and the average ray velocity ($\overrightarrow{W}$). According to Blankenship and Bentley (1987), the average ray velocity ($\overrightarrow{W}$) and angle of incidence ($\sigma'_{\pm}$) for a TI medium underlain by a dipping reflector (dip = β) can be approximated by equations 7 and 8:

$$\overrightarrow{W}_{\pm} = \left\{\frac{4h^2+x^2cos^2\beta}{t^2}\right\}^{1/2} \tag{7}$$

$$\sigma'_{\pm} \cong \tan^{-1}\left\{\frac{x\ \cos\beta}{2h}\right\} \pm \beta \tag{8}$$

Where x is the source-receiver offset in the plane of incidence, h is the thickness of the ice sheet at $x/2$, t is the travel time, and ± indicates the up-going and down-going rays (see figure 29). Using the calculated $\overrightarrow{W}_{\pm}$ and $\sigma'_{\pm}$ it's possible to approximate the coefficients D, E, and F from equation (9) by means of a least squares regression. The resultant D, E, and F incorporate the anisotropy in the medium and are used to generate the slowness vector $\vec{S}_{\pm}$ (equation 10) based on the wave front (equations 11 and 12). The resultant slowness vector $\vec{S}$ is used to calculate the coefficient ψ (equation 11), which represents the change in velocity as a function of angle of incidence. Using the ψ and the angle of incidence ($\sigma'_{\pm}$), we calculated σ, which represents the angle between the axis of symmetry, Z (figure 28), and the direction of wave propagation. The resultant $\vec{S}_{\pm}$ calculated in equation (10) are used to determine the average slowness($\bar{\vec{S}}$) in equation (13). The resultant slowness is compared to the model in equation (6) using multiple ice crystal orientations (figure 27). The ice crystal orientation model that best matches the slowness results is selected as the mean c-axis orientation for the area of study.

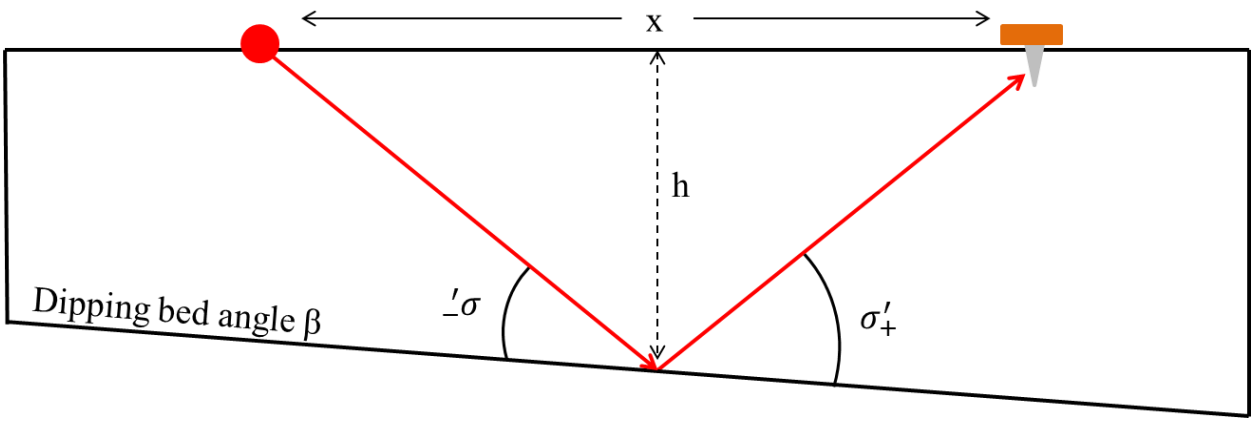

Figure 29: Visual representation of variables necessary for seismic anisotropy analysis.

$$\overrightarrow{W}^{-1} \cong \overline{W^{-1}} \cong D + \frac{1}{2}E(\cos 2\sigma'_- + \cos 2\sigma'_+) + \frac{1}{2}F(\cos 4\sigma'_- + \cos 4\sigma'_+) \quad (9)$$

$$\vec{S}_\pm = D + E\cos 2\sigma'_\pm + F\cos 4\sigma'_\pm \quad (10)$$

$$\tan\psi_\pm = \frac{1}{W}\frac{d\vec{V}}{d\sigma'_\pm} = -\frac{1}{S}\frac{d\vec{S}}{d\sigma} \quad (11)$$

$$\sigma' = \sigma + \psi \quad (12)$$

$$\bar{\vec{S}} = \frac{1}{2}[(S_-) + (S_+)] \quad (13)$$

3.4 Experiment

For the purpose of this investigation, we use a stationary array of eight closely spaced vertical geophones with twenty-two variable offset sources as described in chapter 2.3. The traces from all the vertical plate mounded geophones were stacked in order to improve the signal to noise ratio. Due to the acquisition geometry of the survey, the dataset is not truly common mid-point (CMP) and covers an area of 1600 m. The method developed by Blankenship and Bentley (1987) requires knowledge of the depth and dip angle of the reflecting horizon. Based on the acquisition geometry of the multi-offset gather, we extracted the ice thickness and dip angle for each mid-point shot record for three horizons of interest relative to the corresponding horizons in the seismic profile presented by Horgan et al. (2008) (figure 30). By combining the information of the multi-offset data with the 2D seismic profile, it was possible to calculate the slowness vs. σ for the three interpreted horizons. Analysis of the three horizons allows us to determine where the preferred ice crystal orientation is occurring within the ice column (appendix 2).

Ice temperature has an effect on seismic velocity and seismic attenuation (e.g., Tonn, 1991; Dasgupta and Clark, 1998; Kohnen, 1974). Temperature variations within the ice column translate to a bulk decrease (warm ice) or increase (cold ice) in p-wave velocity. Given that studies using seismic and ice core measurements show a temperate basal ice layer within the lowermost 300 m for the area of study (Peters et al., 2012; Iken et al., 1993) it is necessary to correct the temperature effects for each horizon in order to successfully preform the anisotropy analysis. To compensate for the effects of temperature variation on seismic velocity, velocity correction factors were determined based on the fit of observed data to the slowness model of Bennett (1968). The model by Bennett (1968) is expressed in slowness, and it was developed for

a constant ice temperature of -10^{o} C. Therefore, the sign of each velocity correction factor will provide information of the internal temperature of the ice column, with a positive correction factor indicating warmer ice than -10^{o} C and negative correction factors indicating ice colder than -10^{o} C.

In order to test for the accuracy of the Blankenship and Bentley equations and study the effects of fast (colder) vs. slow (warmer) ice, a 2D model was generated to simulate a 2000 m isotropic ice sheet with a glacial till bed (Vp = 2000 m/s V_S = 1000 m/s ρ = 1.9 g/cm^3). Three CMP synthetic simulations with varying ice velocity (1: Vp = 3780 m/s V_S = 1890 m/s 2: Vp = 3830 m/s V_S = 1915 m/s 3: Vp = 3900 m/s V_S = 1950 m/s and a constant density of 0.91 g/c m^3) were generated. The model was generated by means of a Ricker wavelet with a sampling rate of 0.0005 s using the Omni software (appendix 3). Using the time picks of the synthetic trace and the geometry information from the model, the slowness vs. σ information was calculated. The results from the synthetic were compared to the model by Bennett (1968) using isotropic ice (I=90).

Picking errors represent a significant problem for the study of anisotropic properties, especially with limited data. Small errors in time picks, translate into changes in the shape of the wave front thus introducing significant errors in the reconstruction of the slowness surface. In order to assess the susceptibility of the analysis to picking errors, random Gaussian noise constrained to one wavelength (5 ms) was added to each of the interpreted horizons and used to determine the slowness and σ. This process was repeated one thousand times and the standard deviation as well as the mean was calculated for each horizon (appendix 4). The results for each horizon were compared to the model by Bennett (1968) for the corresponding I of each horizon,

to determine the effect of picking errors in the method and determine the stability of the interpretation using the available data.

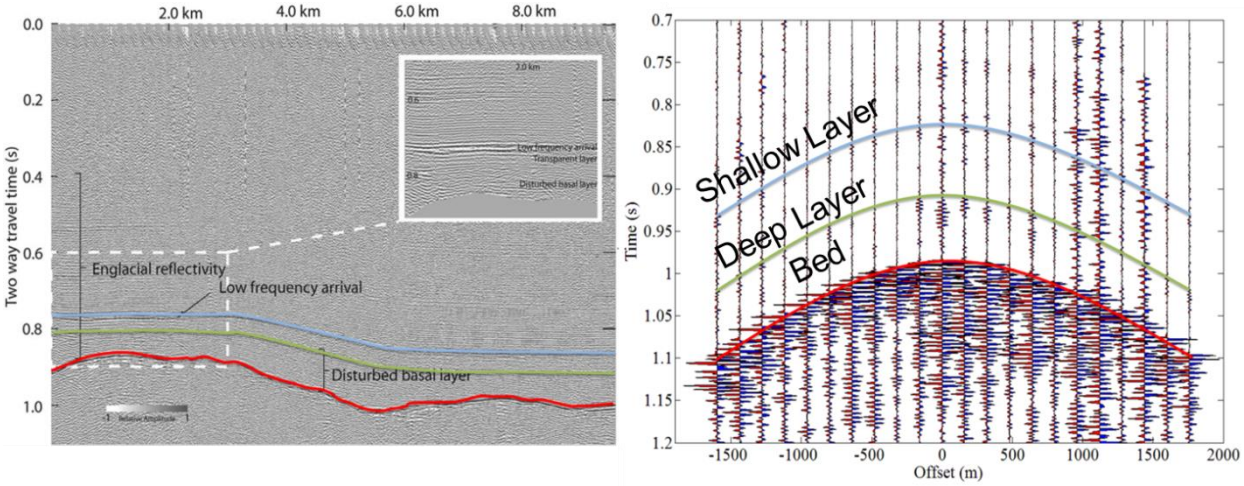

Figure 30: 2D seismic profile collected by Horgan et al., (2008) along flow of the Jakobshavn Glacier (left). Multi-offset data simultaneously collected with 2D (right).

3.5.1 Results

The depth and dip for the bed and two internal layers (shallow and deep: Table 1) were successfully extracted at the midpoint of each trace of the multi-offset data (figure 30: left) using the 2D seismic lines (figure 30: right) collected in the same area of study (Horgan et al., 2008). Using the interpreted depth and dip, combined with the time picks extracted from the multi-offset data for the three interpreted horizons, it was possible to calculate the slowness variation with respect to σ using the method described in section 3.3. The analysis for all three layers revealed that the slowness results match the models of I=33, I =34 and I=70 with correction factors of 90, 125 and 30 m/s for the bed, deep and shallow layers respectively (figure 31-32 and table I).

The synthetic analysis reveals anisotropy of less than 0.1% with offset for all three models. The V_p velocity of 3830 m/s matched the model of Blankenship and Bentley (1987) for isotropic ice. An increase or decrease of velocity (V_p = 3900 and V_p= 3780 respectively) results in a bulk shift of the slowness and does not change the shape of the slowness surface (figure 33).

The arrival time error analysis revealed that the shape of the slowness surface can be susceptible to the time picking. But the analysis of the mean and standard deviation determined by multiple iterations with random Gaussian noise show that the overall trend of the shallow internal layer is representative of isotropic ice (I=70) while the bed (I=33) and deep internal layer (I=35) is characteristic by ice with preferred ice crystal orientation and closely matches the results obtained using the analysis developed by Blankenship and Bentley (1987) (figure 31).

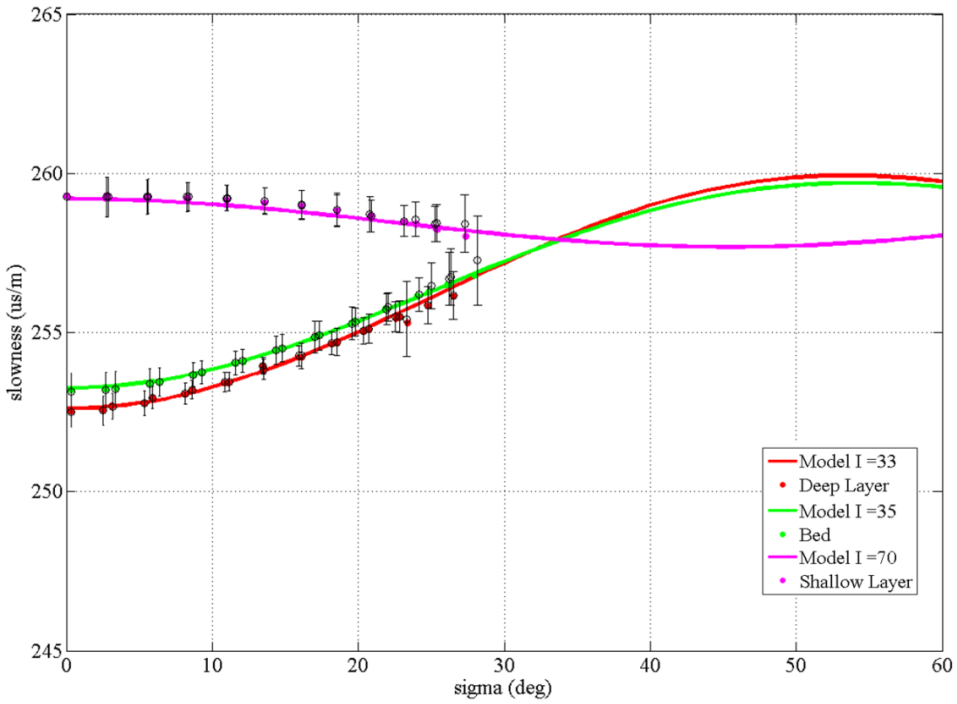

Figure 31: Mean ice crystal orientation results of three interpreted horizons from multi-offset stacked data. Error bars calculated from the standard deviation of multiple iterations of time picks with added random noise.

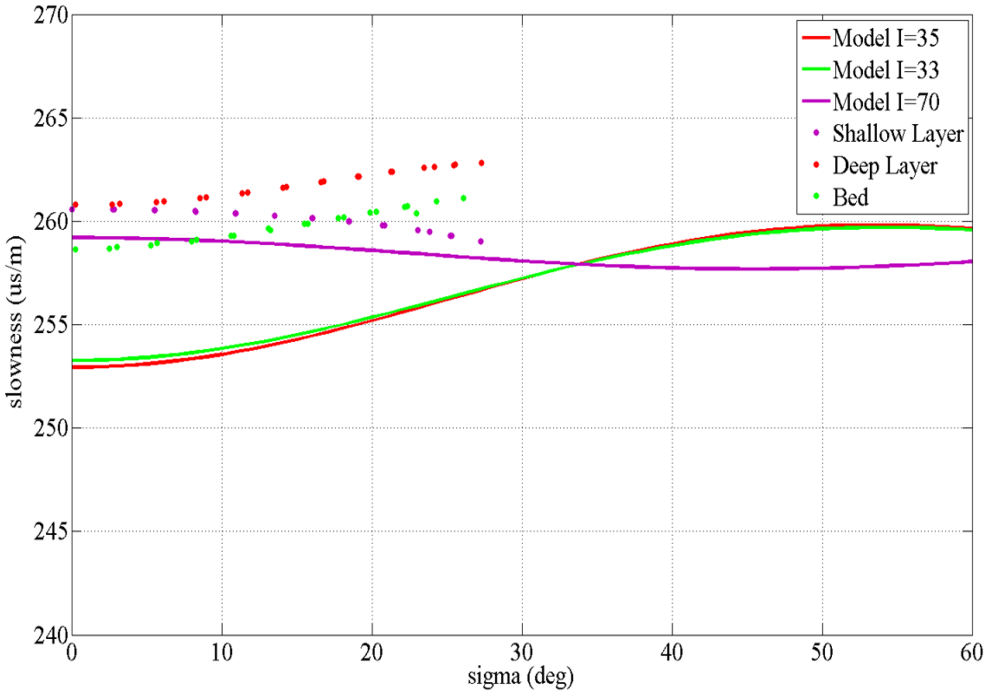

Figure 32: Uncorrected mean ice crystal orientation results of three interpreted horizons from multi-offset stacked data.

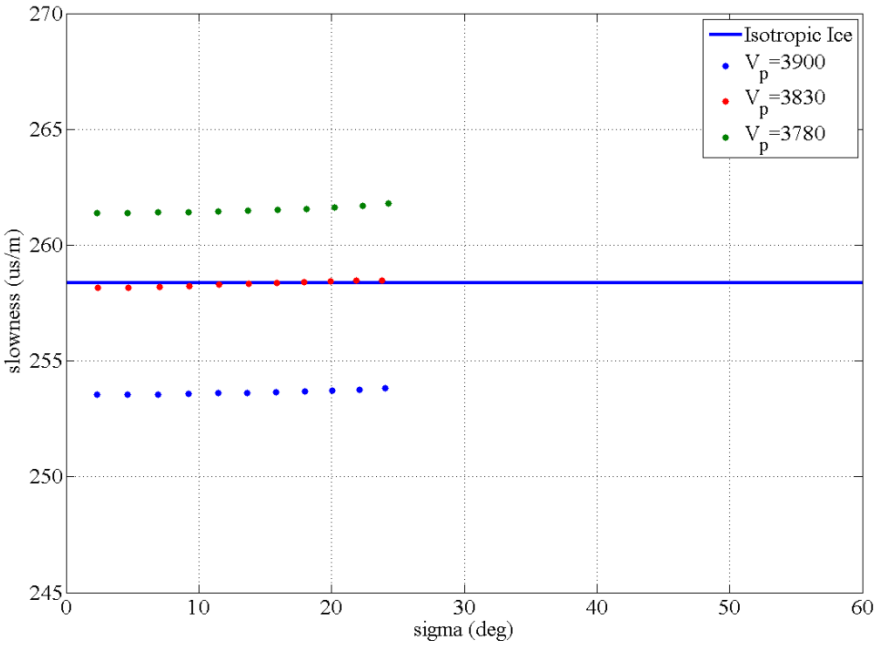

Figure 33: Synthetic analysis results for the three models with multiple velocities.

	Bed					Deep				Shallow			
Offset (m)	Sigma	Slowness	Depth (m)	I=33	Dip	Sigma	Slowness	I = 35	Depth (m)	Sigma	Slowness	I = 70	Depth (m)
1755	26.5	256.2	1900	256.3	0.04	28.0	256.6	256.9	1750	27.4	257.9	258.2	1600
1595	24.8	255.9	1897	255.9	0.03	26.1	256.3	256.5	Dip	25.3	258.1	258.3	Dip
1435	22.8	255.5	1895	255.7	0.01	24.1	256.0	256.1	0	23.2	258.3	258.4	0
1275	20.7	255.2	1894	255.2	0.03	21.9	255.6	255.7		20.9	258.5	258.5	
1115	18.5	254.7	1892	254.6	0.00	19.6	255.1	255.4		18.6	258.7	258.6	
955	16.1	254.3	1892	254.2	0.00	17.0	254.7	254.8		16.1	258.8	258.8	
795	13.5	253.9	1892	253.9	-0.05	14.4	254.2	254.4		13.6	258.9	258.9	
635	10.9	253.5	1896	253.4	-0.05	11.6	253.8	254.1		11.0	259.0	259.0	
475	8.1	253.1	1900	253.0	-0.05	8.7	253.5	253.7		8.3	259.0	259.1	
315	5.3	252.8	1904	252.8	-0.04	5.7	253.2	253.5		5.5	259.1	259.1	
155	2.5	252.6	1907	252.7	0.00	2.7	253.0	253.3		2.7	259.1	259.2	
5	0.3	252.6	1907	252.6	-0.01	0.4	253.0	253.3		0.1	259.1	259.2	
165	3.1	252.8	1908	252.7	-0.05	3.4	253.0	253.3		2.8	259.1	259.2	
325	5.9	253.0	1912	252.9	-0.08	6.4	253.2	253.5		5.6	259.1	259.1	
485	8.6	253.3	1918	253.2	-0.08	9.3	253.5	253.7		8.3	259.0	259.1	
645	11.1	253.5	1924	253.4	-0.04	12.1	253.9	254.1		11.0	259.0	259.0	
805	13.5	254.0	1927	253.9	-0.11	14.8	254.3	254.5		13.6	258.9	258.9	
965	15.9	254.3	1936	254.2	-0.08	17.4	254.7	254.8		16.1	258.8	258.8	
1125	18.2	254.7	1942	254.6	-0.08	19.7	255.2	255.4		18.6	258.7	258.6	
1285	20.4	255.1	1948	255.0	-0.04	22.0	255.6	255.7		20.9	258.5	258.5	
1505	22.6	255.5	1951	255.7	-0.03	24.9	256.1	256.3		24.0	258.3	258.4	
1605	23.4	255.4	1953	255.9	-0.21	26.2	256.3	256.5		25.4	258.1	258.3	

Table 1: Anisotropy results for the three horizons of interest.

3.6 Discussion

The seismic velocity anisotropy model developed by Bennett, (1968) relates the slowness of ice at a temperature of -10^{o} C as a function of ice crystal orientation (I) and the direction of wave propagation (σ). But seismic velocity propagation in ice (Vp) is dependent on temperature (Kohnen, 1974). Therefore, the elastic moduli determined experimentally by Bennett, (1968) and used in the field data analysis developed by Blankenship and Bentley (1987) and used in this investigation, is affected by the ice column temperature. The synthetic analysis in figure 33 shows that the Blankenship and Bentley (1987) technique is sensitive to an increase or decrease in velocity due to a decrease or increase in ice temperature, resulting in a bulk shift of the slowness (decrease in velocity). It is notable that changes in velocity due to temperature variations, do not introduce variations in velocity with offset (figure 33). Therefore, the only likely explanation for slowness variation with offset (figure 31) is preferred ice crystal orientation due to the anisotropic properties of the ice crystal.

Studies using seismic and ice core measurements show a temperate basal ice layer within the lowermost 14% of Jakobshavn Glacier (Peters et al., 2012; Iken et al., 1993). To compensate for the effects of temperature variation on seismic velocity, reflector depth correction factors were determined based on the fit of observed data to the slowness model of Bennett (1968). Given that the model by Bennett, (1968) simulates the slowness response of ice at a temperature of -10^{o} C, positive velocity correction factors would correspond to ice wormer then -10^{o} C and small correction factors would indicate temperatures close to -10^{o} C. The correction factor of 30 m/s for the shallow layer (near offset time arrival 0.82 s) indicated that the top 1640 m of the ice column is characterized by ice with a temperature close to -10^{o} C, while the correction factors of 125 m/s for the deep internal layer and 90 m/s for the bed indicate warmer ice at the bottom 300

m (figure 31-32). This result strongly agrees with the temperature model for the area of study derived by Peters et al. (2012) using seismic attenuation (figure 34).

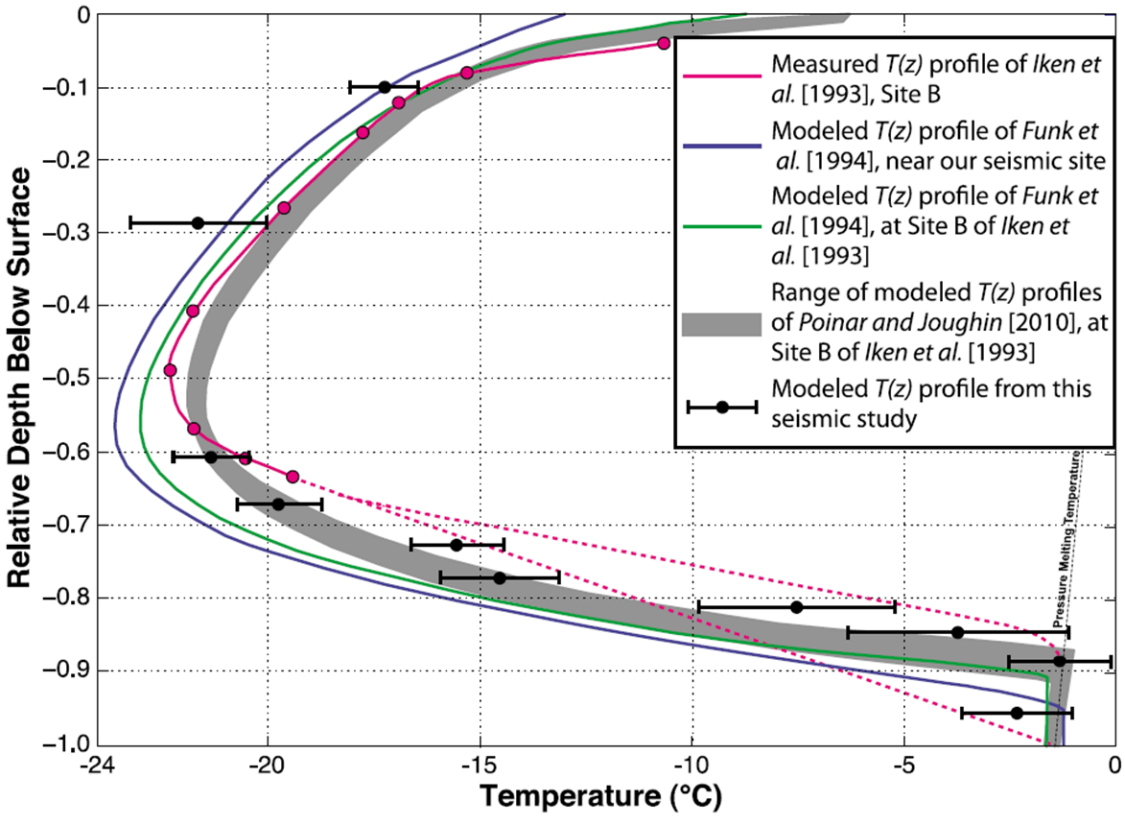

Figure 34: Comparison of calculated temperature profile based on seismic attenuation by Peters et al., 2012, en-glacial temperature observations by Iken et al. (1993) and modeled temperature profiles of Funk et al. (1994) as well as Poinar and Joughin (2010).

Using the velocity correction factors, the seismic anisotropy results of this investigation suggest that the top 1640 m correspond to ice with isotropic ice (I=70), while the bottom 300 m is characterized by anisotropic ice (average I=34). However, multi-azimuth data is necessary to capture the full radial extent of velocity anisotropy in an ice column. Given that the 2D multi-offset data was collected along the flow direction of the glacier, the results from the analysis using the method from Blankenship and Bentley (1987) would only correspond to the anisotropy along the 2D line which does not necessarily indicate the mean anisotropy in the ice column. The

location of the area of study is approximately 70 km away from the mouth of the Jakobshavn glacier and the ice is moving at approximately 155 m a^{-1}. Therefore it is reasonable to assume that lateral drag is small and the main driving forces acting in the ice column are basal drag and gravitational forces. Typically in areas were vertical sheer is dominant the near surface ice is characterized by a random c-axis distribution while the basal ice is characterized by preferred ice crystal orientation (e.g., Wang et al., 2002; Alley, 1988; Budd and Jacka, 1989). Using an age–depth relationship (Funk et al., 1994) and knowledge of the impurity loading history of Greenland (Mayewski et al., 1993; O'Brien et al., 1995), Horgan, et al., (2008) suggested that the low frequency arrival at 1650 m (figure 30) corresponds to the bottom of the Younger Dryas stadial ice, characterized by predominantly vertical c-axes. Therefore the results of this investigation strongly agree with the observations made by Horgan, et al., (2008).

As previously discussed, the Bennett, (1968) model is based on single ice crystal ultrasonic measurements. This model does not necessary incorporate the complexity of seismic wave propagation through an ice sheet or glacier. Therefore the I values calculated in this investigation for each layer should be used to determine the presence of preferred ice crystal orientation and not to quantify the actual angle at which the ice crystals are oriented.

3.7 Conclusions

Analysis of the seismic wave slowness variability as a function of wave field angle was used successfully at the Jakobshavn Glacier to determine ice crystal orientation characteristics. A shallow internal ice layer was imaged at a depth of 1640 km. The bed varied in depth from 1900 m to 1953 m with dip angles ranging from 0 to 6 degrees (figure 35). The anisotropy analysis (figure 32) revealed that the shallow internal layer exhibits minor changes in slowness suggesting isotropic ice, while the velocity correction factor of 30 m/s applied to the shallow layer indicates that the average ice temperature from the surface to 1640 m is close to -10^{o} C (figure 35). Analyses of the bed and deep internal layer reflectors show slowness variation with offset and large correction factors (90 and 125 m/s respectively) indicating anisotropic ice with temperatures warmer than -10^{o} C (figure 35). Therefore we conclude that the upper 1640 m of the ice column consists mostly of colder (≈ -10^{o} C) isotropic ice with the lower 300 m of the ice column characterized by warmer ice (> -10^{o} C), with preferred ice crystal orientation (figure 35). This result strongly agrees with the englacial reflectivity observations reported by Horgan et al. (2008) and the ice column temperatures reported for areas near the Jakobshavn Glacier (Peters et al., 2012; Iken et al., 1993).

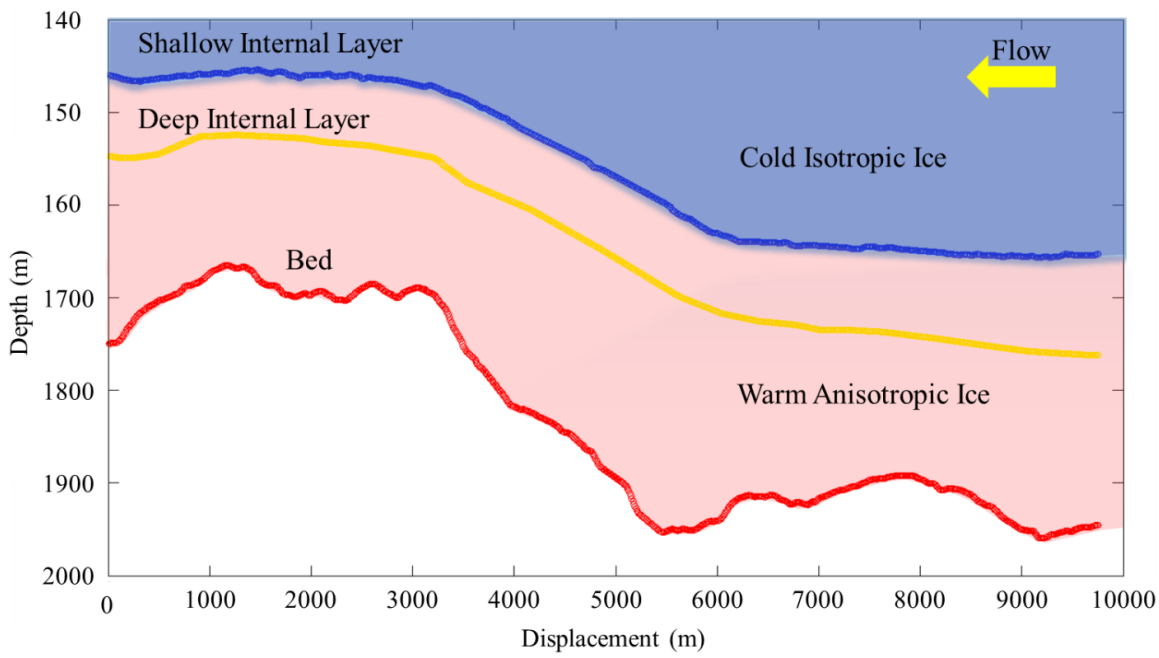

Figure 35: Ice column model based on anisotropy analysis. Layer depth interpreted by Horgan et. al., (2008).

4.0 References

Alley, R. B. (1988), Fabrics in polar ice sheets: Development and prediction, *Science, 240, 493–495.*

Al-Zayer, R. M., (2010), Modeling the Near-Surface Using High-Resolution Seismic Data, *PhD thesis, Thesis University of Kansas.*

Anandakrishnan, S., S. V. Smith, A. M. Stoffa. and I. W. D. Dalziel (1995), A multifold high resolution seismic reflection profile in central west Antarctica, *in VII Int. Symp. On Antarctic Earth Sciences, Abstract, p. 5, Univerista degli Studi di Siena, Siena, Italy.*

Anandakrishnan, S., (2003), Dilatant till layer near the onset of streaming flow of Ice Stream C, West Antarctica, determined by AVO analysis, *Ann. Glaciol* 36 2003.

Azuma, N., Y. Wang, K. Mori, H. Narita, T. Hondoh, H. Shoji, and O. Watanabe (1999), Textures and fabrics in the Dome F (Antarctica) ice core, *Ann. Glaciol., 29, 163– 168.*

Bennett, H. F., (1968), An investigation into velocity anisotropy through measurements of ultrasonic wave velocities in snow and ice cores from Greenland and Antarctica, *PhD thesis, Univ. of Wis.-Madison, Madison.*

Bentley, C. R. (1971), Seismic evidence for moraine within the basal Antarctic ice sheet, in Antarctic Snow and Ice Studies II, *Antarct. Res. Ser., vol. 16, edited by A. P. Crary, pp. 89–129, AGU, Washington, D. C.*

Bentley, C. R. (1986), P-Wave Anisotropy in the high polar ice of east Antarctica, *Master thesis, Univ. of Wis.-Madison, Madison.*

Blankenship, D. D., and C. R. Bentley (1987), The crystalline fabric of polar ice sheets inferred from seismic anisotropy, *The Physical Basis of Ice Sheet Modeling. IAHS Publ. no. 170.*

Budd, W. F., and T. H. Jacka (1989), A review of ice rheology for ice sheet modeling, Cold Reg, *Sci. Technol., 16, 107– 104.*

Church J.A., J.M. Gregory, P. Huybrechts, M. Kuhn, K. Lambeck, M.T. Nhuan, D. Qin, and P.L. Woodworth, (2001), Changes in Sea Level, in Climate Change 2001, *The Scientific Basis,* eds. Houghton and Ding, Cambridge Univ. Press, Cambridge.

Cuffey, K. M., and W. S. B. Paterson (2010), The Physics of Glaciers, 4th ed., Elsevier, New York.

Csatho, B., T. Schenk, C.J. Van der Veen, and W. B. Krabill (2008), Intermittent thinning of Jakobshavn Isbræ, West Greenland, since the Little Ice Age, *J. Glaciol., 34(116), 131-144.*

Dahl-Jensen, D., and N.S. Gundestrup (1987), Constitutive properties of ice at Dye 3, Greenland, *The Physical Basis of Ice Sheet Modelling*. IAHS Publ. no. 170.

Dasgupta, R., and R. A. Clark (1998), Estimation of Q from surface seismic reflection data, Geophysics, 63(6), 2120–2128.

Diprinzio, C., L. Wilen, R. Alley, J. Fitzpatrick, M. Spencer, and A. Gow (2005), Fabric and texture at Siple Dome, Antarctica, *J. Glaciol., 51(173), 281–290.*

Eiken, O., M. Degutsch P. Riste and K. Rod (1989), Snowstreamer: an efficient tool in seismic acquisition, 374/First Break Vol7, No 9, September 1989.

Einarsson, D., L. Brooks, G. Bennett, and A. White (1977), Seismic Survey on the Beauford Sea ice, *Geophysics, 42, 148.*

Funk, M., K. A. Echelmeyer, and A. Iken (1994), Mechanisms of fast flow in Jakobshavns Isbræ, West Greenland: Part II. Modeling of englacial temperatures, *J. Glaciol., 40(136), 569– 585.*

Gillet-Chaulet, F., O. Gagliardini, J. Meyssonnier, T. Zwinger, and J. Ruokolainen (2006), Anisotropy in polar ice and related ice-sheet flow modeling, *J. Non-Newtonian Fluid Mech., 134, 33–43*

Galperin, Y. I. (1955), Azimuthal method of seismic acquisition, GosKomIzdat.

Galperin, Y. I. (1974), Vertical seismic profiling, *SEG Special Publication, Tulsa.*

Gogineni, S., T. Chuah, C. Allen, K. Jezek and R. K. Moore (1998), An improved coherent radar depth sounder, *J. Glaciol., 44(148), 659–669.*

Gogineni, S. and 9 others. (2001), Coherent radar ice thickness measurements over the Greenland ice sheet, *J. Geophys. Res., 106(D24), 33,761–33,772.*

Gow, A. J., D. A. Meese, R. B. Alley, J. J. Fitzpatrick, S. Anandakrishnan, G. A. Woods, and B. C. Elder (1997), Physical and structural properties of the GISP2 ice cores, *J. Geophys. Res., 102(C12), 26,559– 26,576.*

Gow, A., and D. Meese (2007), Physical properties, crystalline textures and c-axis fabrics of the Siple Dome (Antarctica) ice core, *J. Glaciol., 53(183), 573–584.*

Graizer, V., (2009), The Response to Complex Ground Motions of Seismometers with Galperin Sensor Configuration. *Bulletin of the Seismological Society of America May 2009 99:1366-1377.*

Herron, S. L., and C.C. Langway (1982), A comparison of ice fabrics and textures at Camp Century, Greenland, and Byrd Station, Antarctica, *Ann. Glaciol.* 3, 118-124.

Herron, S.L., C.C. Langway, and K.A. Brugger (1985), Ultrasonic velocities and crystalline anisotropy in the ice core from Dye 3, Greenland. In: *Greenland Ice Core: Geophysics, Geochemistry, and the Environment*, 23-31. Geophysical Monograph 33, American Geophysical Union, Washington, D.C., USA.

Horgan, H. J., S. Anandakrishnan, R. B. Alley, L. E. Peters, G. P. Tsoflias, D. E. Voigt, and J. P. Winberry (2008), Complex fabric development revealed by englacial seismic reflectivity: Jakobshavn Isbræ, Greenland, *Geophysical Research Letters. Vol. 35, L10501*

Horgan, H. J., S. Anandakrishnan, R. B. Alley, and L. E. Peters (2011), Englacial seismic reflectivity: imaging crystal-orientation fabric in West Antarctica, *Journal of Glaciology, Vol. 57, No. 204.*

Hooke, R. L., (1981), Flow law for polycrystalline ice in glaciers: Comparison of theoretical predictions, laboratory data, and field measurements, *Rev. Geophys., 19(4), 664–672.*

Hoover, G. M., and J. T. O'Brien (1980), The influence of the planted geophone on seismic land data: *Geophysics, v. 45, p. 1239-1253. Lamar, A., 1970, Geophone-ground coupling: Geophys. Prosp., v. 18, p. 300-319.*

Huybrechts, P., and J. Oerlemans (1988), Evolution of the East Antarctic ice sheet: A numerical study of thermo-mechanical response patterns with changing climate, *Ann. Glaciol., 11, 52–59.*

Iken, A., K. Echelmeyer, W. Harrison, and M. Funk (1993), Mechanisms of fast flow in Jakobshavn Isbrae, West Greenland; part I: Measurements of temperature and water level in deep boreholes, *J. Glaciol., 39, 15–25.*

Joughin, I., B. Smith, I. Howat, and T. Scambos (2010), MEaSUREs Greenland Ice Sheet Velocity Map from InSAR Data, *Boulder, Colorado, USA: National Snow and Ice Data Center. Digital media*

Joughin, I., B. E. Smith, I. M. Howat, D. Floricioiu, R. B. Alley, M. Truffer, M. Fahnestock, M. Truffer, and M. Fahnestock (2012), Seasonal to decadal scale variations in the surface velocity of Jakobshavn Isbrae, Greenland: Observation and model-based analysis, *J. Geophysical Research, Vol. 117.*

King, E. C., and A. C. Bell (1996), A Towed geophone system for use in snow-covered terrain, *Geophys. J. Int. (1996) 126, 54-62.*

Kohnen, H. (1974), The temperature dependence of seismic waves in ice, *J. Glaciol., 13, 144–147.*

Kruppenbach, J. A., and J. W. Bedenbender (1976), Towed land cable US patent no. 504590

Matsuoka, K., T. Furukawa, S. Fujita, H. Maeno, and S. Uratsuka (2003), Crystal orientation fabrics within the Antarctic ice sheet revealed by a multi-polarization plane and dual-frequency radar survey, *J. of Geophysical Research, Vol. 108, NO. B10, 2499.*

O'Brien, S., P. Mayewski, L. Meeker, D. Meese, M. Twickler, and S. Whitlow (1995), Complexity of Holocene climate as reconstructed from a Greenland ice core, Science, 270, 1962– 1964.

Kohnen, H., (1974), The Temperature Dependence of seismic wave in ice, *Jornal of Glaciology, Vol 13 No. 67.*

Love, A. E. H., A treatise on the mathematical theory of elasticity. Dover Publications, New York. First American Printing 1944, fourth edition, 1927.

Mayewski, P. A., L. D. Meeker, S. Whitlow, M. S. Twickler, M. C. Morrison, R. B. Alley, P. Bloomfield, and K. Taylor (1993), The atmosphere during the Younger Dryas, *Science, 261, 195– 197.*

Peters, L., S. Anandakrishnan, R.B. Alley, and D. E.Voigt (2012a), Subglacial sediments as a control on the onset and location of two Simple Coast ice streams, West Antarctica. *J. Geophysical Research, Vol. 111, B01302, doi:10.1029/2005JB003766.*

Peters, G. P., S. Anandakrishnan, R. B. Alley, and D. E. Voigt (2012b), Seismic attenuation in glacial ice: A proxy for englacial temperature, *J. Geophysical Research, Vol. 117, F02008, doi:10.1029/2011JF002201*

Poinar, K. E., and I. Joughin (2010), Temperate ice under Jakobshavn Isbrae and other Greenland glaciers, *Abstract C23B-0606 presented at 2010 Fall Meeting, AGU, San Francisco, Calif., 13–17 Dec.*

Portnov, V.G., N.I. Barkov, and N.A. Korableva (1980), Orientation of optical axes of ice crystals from Vostok Station ice cover. *Informatsionnyi Biulletin', Sovetskaia Antarkticheskaia Ekspeditsiia 100, 70-74 (in Russian).*

Rignot, E. and P. Kanagaratnam (2006), Changes in the velocity structure of the Greenland Ice Sheet. *Science, 311(5673), 986–990.*

Röthlisberger, H., (1972), Seismic exploration in cold regions, *technical report, Cold Reg. Res. and Eng. Lab, Hanover, N. H.*

Russell-Head, D.S. and W.F. Budd (1979), Ice-sheet flow properties derived from bore-hole shear measurements combined with ice-core studies. *Glaciol. 24(90), 117-130.*

Sen, V., P. L. Stoffa, I. Dalziel, D., D. Blankenship, A. M. Smith, and S. Anandakrishnan (1998), Seismic Surveys in Central West Antarctica: Data and Processing Examples from the Antalith Field Tests (1994-1995). *Terra Antarctica 1998, 5(4), 761-772.*

Sheriff E. R., (2006), Encyclopedic Dictionary of Applied Geophysics, 4nd ed., Tulsa OK, Press, Society of Exploration Geophysics.

Shoji, H., and C.C. Langway (1988), Flow-Law Parameters of the DYE 3, Greenland, Deep Ice Core, *Annals of Glaciology 10 1988.*

Tonn, R., (1991), The determination of seismic quality factor Q from seismic data, *Geophys. Prospect., 39, 1–27.*

Thomas, R.H., (2004), Force-perturbation analysis of recent thinning and acceleration of Jakobshavn Isbræ, Greenland, *J. Glaciol. 50(168), 57–66.*

Thorsteinsson, T., J. Kipfstuhl, and H. Millar (1997), Textures and fabrics in the GRIP ice core, *J. Geophys. Res., 102(C12), 26,583– 26,599.*

Tsvankin, I., (2005), Seismic signatures and analysis of reflection data in anisotropic media, Vol 29 ., 7-13 pp., Colorado School of Mines. Press, New York.

Van der Veen, C.J., J.C. Plummer, and L.A. Stearns (2011), Controls on the recent speed-up of Jakobshavn Isbræ, West Greenland, *J. Glaciol., 57(204), 770-782.*

Van der Veen, C.J., (2001), A need for more realistic ice-sheet models, *SCAR, 30. Nov 2007*

Van der Veen, C.J., and I. M. Whillans (1994), Development of fabric in ice, *Cold Regions Science and Technology, (22) 171-195.*

Wang, Y., T. Thorsteinsson, J. Kipfstuhl, H. Miller, D. Dahl-Jensen, and H. Shoji (2002), A vertical girdle fabric in the NorthGRIP deep ice core, north Greenland, *Ann. Glaciol., 35, 515– 520.*

Appendix I : Galperin rotation code

```
% rotate Galperin mounts

function OUT = Grotate(IN)

Data = IN;
store = zeros(length(Data(:,1)),3);

for n_sample = 1:1:length(Data(:,1));
    store(n_sample,1) = [sqrt(1/3)]*[Data(n_sample,1)] +
[sqrt(1/3)]*[Data(n_sample,2)] + [sqrt(1/3)]*[Data(n_sample,3)];
    store(n_sample,2) = [sqrt(2/3)]*[Data(n_sample,1)] -
[sqrt(1/6)]*[Data(n_sample,2)] - [sqrt(1/6)]*[Data(n_sample,3)];
    store(n_sample,3) = [        0]*[Data(n_sample,1)] +
[sqrt(1/2)]*[Data(n_sample,2)] - [sqrt(1/2)]*[Data(n_sample,3)];
end

Data(:,1) = store(:,1); Data(:,2) = store(:,2); Data(:,3) = store(:,3);

OUT = Data;

end
```

Appendix II: Blankenship & Bentley analysis

```
clear; clc;

%-------------------------------------------------------
% Analysis of Greenland 2007, P-wave reflection data
% Data corrected for elevation in SPW, times picked in Matlab

load Bed;   %Load Horizon Time Picks and Offset

x=offsettime(1:22,1);
t=offsettime(1:22,2);

figure(1)
plot(x,-t),xlabel 'offset (m)',ylabel '2-way time (s)',grid
title 'Bed Picks'; y=x; x=abs(x);

% use eqs. 8 & 9 to compute WW (<W> average ray velocity) and sigp (sigma
prime + / -)

correccion=55; % Correccion Factor
ll=ll+correccion;

for l=1:length(x)
h=ll(l);
b=Dip(l);
WW(l)=sqrt((4*h^2 + x(l)^2*cos(b)^2)/t(l)^2);
sigpplus(l)=atan((x(l)*cos(b))/(2*h))-b;
sigpminus(l)=atan((x(l)*cos(b))/(2*h))+b;
```

```
end

% follow methodology described in page 21 to transform WW and sigp's to S
% (slowness) and sigma

% step 1
WWinv=D+0.5*E*(cos(2*sigpminus)+cos(2*sigpplus))+0.5*F*(cos(4*sigpminus)+co
%s(4*sigpplus)) [eqs 15]
x1=0.5*(cos(2*sigpminus)+cos(2*sigpplus));
x2=0.5*(cos(4*sigpminus)+cos(4*sigpplus));
X = [ones(size(WW')) x1' x2'];
WWinv=1./WW;
z = X\WWinv';
D=z(1);
E=z(2);
F=z(3);

% step 2: use coefficients from step 1 to compute W using eqs 10
Winvplus=D+E*cos(2*sigpplus)+F*cos(4*sigpplus);
Wplus=1./Winvplus;
Winvminus=D+E*cos(2*sigpminus)+F*cos(4*sigpminus);
Wminus=1./Winvminus;

% use eqs 2 to compute psi

npts=length(x);
for i=1:npts-1
    psisigmap(i)=(Wplus(i+1)-Wplus(i))/(sigpplus(i+1)-sigpplus(i));
    psisigmam(i)=(Wminus(i+1)-Wminus(i))/(sigpminus(i+1)-sigpminus(i));
end
psisigmap(npts)=psisigmap(npts-1);
psisigmam(npts)=psisigmam(npts-1);

for i=1:npts
    psip(i)=atan((Winvplus(i))*psisigmap(i));
    psim(i)=atan((Winvminus(i))*psisigmam(i));
end

% step (3) use eqs 1 to comute sigma
   sigmap= sigpplus- psip;
   sigmam= sigpminus- psim;
% step (4), compute slowness SS from field data

for i=1:npts
Winv(i)=0.5*(Winvplus(i)+Winvminus(i));     % eqs 11
SS(i)=Winv(i)*(0.5*(1/cos(psim(i))+1/cos(psip(i)))); % eqs 13 & 14
end

%-------------------------------------------------
% repeat steps 2 to 4 without the regression step 1 to compute again SSS
% use WW instead of Wplus above
% use eqs 2 to compute psi

WWinv=1./WW;
npts=length(x);
```

```
for i=1:npts-1
    psisigmap(i)=(WW(i+1)-WW(i))/(sigpplus(i+1)-sigpplus(i));
    psisigmam(i)=(WW(i+1)-WW(i))/(sigpminus(i+1)-sigpminus(i));
end

psisigmap(npts)=psisigmap(npts-1);
psisigmam(npts)=psisigmam(npts-1);

for i=1:npts
    psip(i)=atan((Winvplus(i))*psisigmap(i));
    psim(i)=atan((Winvminus(i))*psisigmam(i));
end

   % step (3) use eqs 1 to comute sigma
   sigmapWW= sigpplus- psip;
   sigmamWW= sigpminus- psim;

   % step (4), compute slowness SS from field data
for i=1:npts
%Winv(i)=0.5*(Winvplus(i)+Winvminus(i));     % eqs 11
SSS(i)=Winv(i)*(0.5*(1/cos(psim(i))+1/cos(psip(i)))); % eqs 13 & 14
end

%-------------------------------------------------------------
% SSav=A'+0.5*B'*(cos(2*sigmam)+cos(2*sigmap))+0.5*C'*(cos(4*sigmam)+co
%s(4*sigmam)) [eqs 16]
U1=0.5*(cos(2*sigmam)+cos(2*sigmap));
U2=0.5*(cos(4*sigmam)+cos(4*sigmap));
U = [ones(size(SS')) U1' U2'];
n = U\SS';
Ap=n(1);
Bp=n(2);
Cp=n(3);

SSav=Ap+Bp*U1+Cp*U2;
sigmaav=(sigmam+sigmap)/2;

%-------------------------------------------------
% Model of slowness vs. sigma (figure 2) and compare to field SS
% define empririically derived coeffs. for -10C ice
% compute eqs 4

a=256.28;
b=-5.08;
c=-5.92;

Icap=[0,10,20,30,40,50,60,70,80,90]*pi/180;
sigma=[0:60]*pi/180;
for k=1:length(Icap)
    I=Icap(k);
    A(k)=(a-b/3-c/15)+(b-
23*c/20)*(cos(I)+cos(I)^2)/6+9*c*(cos(I)^3+cos(I)^4)/40;
    B(k)=(b-c)*(cos(I)+cos(I)^2)/2+c*(cos(I)^3+cos(I)^4)/2;
    C(k)=-3*c*(cos(I)+cos(I)^2)/8+7*c*(cos(I)^3+cos(I)^4)/8;
    BC(k)=B(k)/C(k);
```

```
end

for k=1:length(Icap)     % eqs 4a
    for l=1:61
    S(k,l)=A(k)+B(k)*cos(2*sigma(l))+C(k)*cos(4*sigma(l));
    end
end

figure(2)                % generate figure 2
for k=1:length(Icap)
plot(sigma*180/pi,S(k,:))
hold on
end

plot(sigmaav*180/pi,SSav*10^6,'g.')
%plot(sigmap*180/pi,SS*10^6,'r',sigmapWW*180/pi,SSS*10^6,'o',sigmaav*180/pi,S
Sav*10^6,'g.')
axis([0 60 240 270]),%legend('model slowness','regression computed
slowness','non-regression slowness','average slowness eq 16')
xlabel 'sigma (deg)', ylabel 'slowness (us/m)',grid
title 'Bed Layer 35 degrees'
hold off
```

Appendix III: Isotropic model

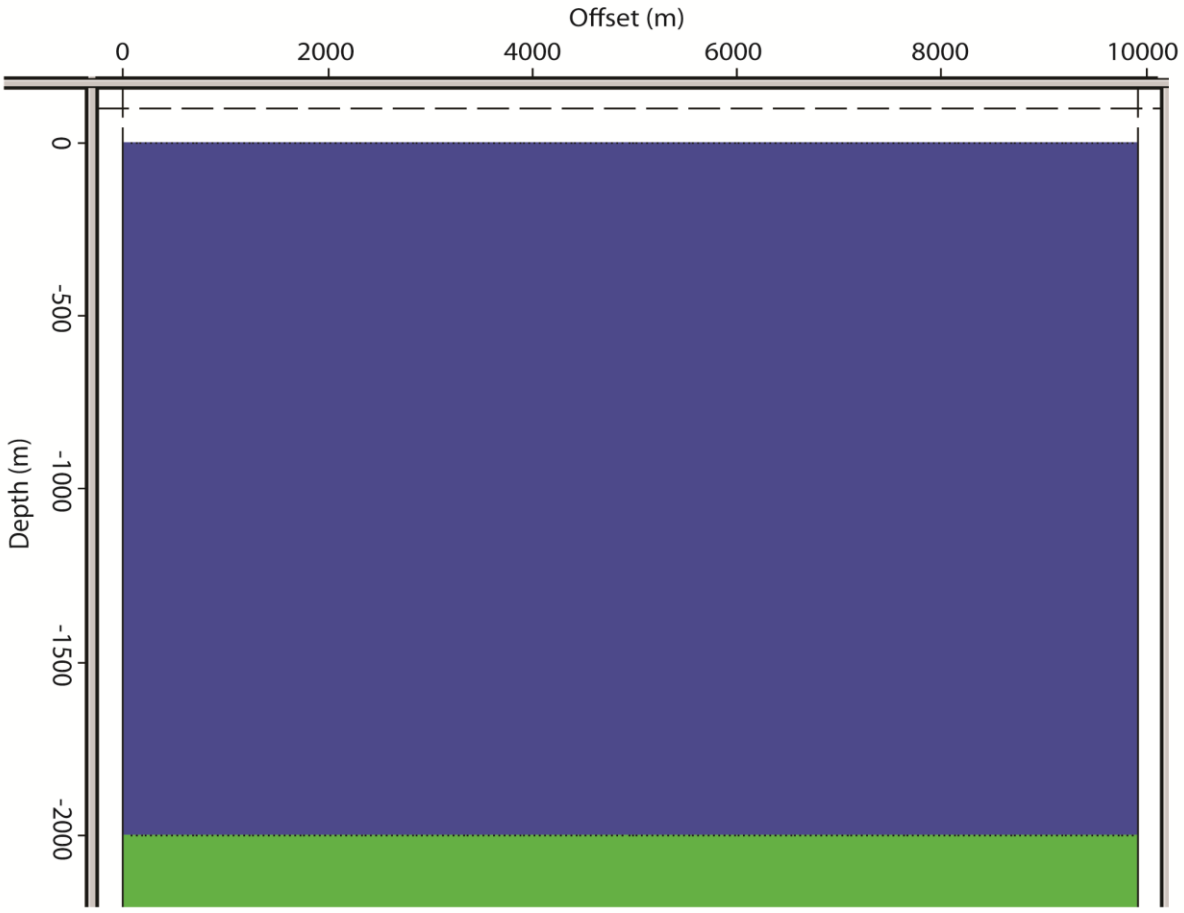

Appendix IV: Mean slowness and sigma values calculated from 1000 iterations picks with Gaussian noise constrained to one wavelet (5 ms) for the three horizons of interest

Bed		Deep		Shallow	
Sigma Mean	Slow Mean	Sigma Mean	Slow Mean	Sigma Mean	Slow Mean
26.5402524	256.4909312	27.88126353	256.9480161	27.49259507	258.3296418
24.774668	256.1607821	26.0292502	256.4300542	25.4071315	258.2973425
22.833614	255.8057411	24.02094082	255.9622104	23.22406947	258.3677637
20.7345952	255.4175972	21.85160314	255.5292763	20.94445436	258.5071727
18.5094593	255.0114867	19.52015612	255.1135488	18.57069271	258.6774565
16.0919965	254.5740548	17.02995778	254.7005259	16.10686636	258.8428469
13.513947	254.1573675	14.38958545	254.2852015	13.55911754	258.9760513
10.8643256	253.7556605	11.61348603	253.8772605	10.93602803	259.0628999
8.13728248	253.4038326	8.722304464	253.5027255	8.248874952	259.1042919
5.35312815	253.0915621	5.742668276	253.1997095	5.511633765	259.1139449
2.52960365	252.8752265	2.722295635	253.0087929	2.738070937	259.1116883
0.33826747	252.8359	0.351872747	252.9552622	0.046162621	259.1122777
3.14424435	253.0070046	3.395502048	253.0475209	2.830121557	259.1204476
5.87951042	253.278464	6.389656875	253.2668154	5.593022814	259.126351
8.59915919	253.5291644	9.302745027	253.5791708	8.317989369	259.1123733
11.1278105	253.7761329	12.10810191	253.9469969	10.9901473	259.0618613
13.4758915	254.2685405	14.7848051	254.3403555	13.5969501	258.9672791
15.9176514	254.5823632	17.31782613	254.7431138	16.12821441	258.8347078
18.1948169	254.9721228	19.69771048	255.1534406	18.57596848	258.6842568
20.3643819	255.3619225	21.89261079	255.5827933	20.90402054	258.5561003
22.573391	255.803872	24.76495017	256.2110384	24.05540579	258.4256731
23.3579074	255.7773724	26.11017783	256.4773139	25.50855672	258.3268528